

Reply to the comments

We thank the two anonymous referees for their kind evaluation of the manuscript. The comments helped us add necessary information and clarifications. Please find our answers (blue text) to the comments (black text) below. Respective changes to the manuscript are indicated in blue in the version attached to this reply. Line numbers in our answers refer to this manuscript version. Tracked changes do not include minor corrections of spelling/grammar not related to the referee comments.

Anonymous Referee #1

Overall this is a solid paper describing the HETEAC aerosol optics/mixing model that is used to aid in EarthCARE algorithm, development. As the authors note, EarthCARE is unique among satellite systems in its high degree of multi sensor integration in deriving aerosol products. Therefore, algorithm developers need a beginning baseline to ensure all of the systems are using compatible models. In and of itself, I think the paper does exactly what it sets out to do: explaining the model, the rationale for why they made the decisions they did, and provide some theoretical uncertainties. From a science reviewer point of view, there is not much to say. Given this is a baseline, they are keeping it all rather simple at this point. They are projecting against the major sources in a logical manner and compare well with observations and existing optical models such as OPAC.

I only suggest minor revisions in a few areas. Going through the paper, I made many notes when the authors massively oversimplified the discussion. I am ok with a simple model as necessity dictates, but the authors need to be clear what the implications of the simplifications are so users can sequester uncertainty. However, the conclusion covers nearly all of my distress (no longer necessary to write them down here)-especially on mixing state which I was most concerned about (which makes the section not really the conclusions). So the paper is at times at odds between declarative statements made throughout, and then in the conclusion waving the hands. Therefore, my only suggestion is to move a lot of that material forward, and perhaps make it an early section. State essentially that for necessity, you have a simple model, but simple models are, well, simple. That is ok with what you want to do.

We thank the referee for bringing these incongruities up. It was indeed a difficult decision where to put which discussion when writing the paper. Simplifications and their implications need to be explained, of course, but we also didn't like to disturb the flow in describing the model itself too much. As a compromise, we have now introduced an additional discussion section (Sect. 8), separated from the shorter conclusion and outlook section (Sect. 9). In Sect. 8, we indicate the different aspects of the discussion by introducing respective subsections, and we also added additional points that were brought up by the referees. We refer to the new Sect. 8 at corresponding places in the paper to make the reader aware of the further discussion.

Other minor things that the authors may want to emphasize is

1) these models probably will not be great for haze events such as in China or India;

This is true. We included the aspect in the discussion in Sect. 8.2 (lines 683-684).

2) use of the lidar ratio is dependent on having a good retrieval, which for lower concentrations is not a given;

The reviewer is correct here, the lidar ratio can only be used for typing when it is retrieved with useful accuracy. For aerosols, roughly speaking, it is expected that useful layer-average lidar-ratio retrievals (SNR of the retrieval better than 100 %) can be done for minimum extinction values on the order of $5.0e-6 \text{ m}^{-1}$ on the 50-100 km horizontal scale. A detailed description of the applied averaging schemes is provided in the paper by Donovan et al.: “The ATLID L2a profile processor (A-AER, A-EBD, A-TC and A-ICE products)”, which will be submitted to the Special Issue soon. We added some text in Sect. 7.2.1 (lines 567-572, see also reply to comment 13 of Referee #2).

3) practically “dusty smoke” have long been the CALIOP’s go to for “We don’t know what this is really.” How will you handle such uncertainty across platforms.

As described in more detailed below (see reply to comment 12 of Referee #2) , we believe that it will take quite some effort to harmonize the long-term data sets. Indeed, the “dusty smoke” class is similar to the “polluted dust” type defined for CALIPSO, and it mainly stands for mixtures of dust with aerosols from combustion processes. Similarly, the “dusty mix” in A-TC and the “dusty marine” type of CALIPSO represent a mixture of dust with weakly or non-absorbing coarse-mode particles, in particular sea salt. The challenge for the harmonization will be to set the boundaries between the pure and the mixed types appropriately to allow for a comparable classification. Here, we will need support from long-term ground-based validation measurements at multiple wavelengths (to cover both ATLID and CALIOP) as well as statistical evaluations of the long-term data sets to adjust them to each other. We added some discussion on the required future efforts in the conclusion and outlook section (lines 757-771).

Other than these I wish the authors well.

Thank you very much!

Anonymous Referee #2

This is a very nice paper describing the model to be used for tropospheric aerosol classification associated with the ATLID and MSI measurements to be acquired during the EarthCARE mission. The paper provides a good description of how the aerosol components were determined, the aerosol optical and physical characteristics of these components, and how they are combined and used to provide aerosol types from the ATLID measurements. The manuscript provides several Figures and Tables to describe these items and an example applied to simulated data. The model should be a good starting point for the EarthCARE aerosol classification. The authors correctly note that this scheme should preserve the CALIOP aerosol types as much as possible in order to facilitate long-term investigations using data from both missions. Along those lines, as noted in comments below, it would be helpful if additional information were provided to determine how the aerosol optical and microphysical characteristics of aerosol types associated with ATLID classification compare with those associated with the CALIOP aerosol types. I recommend publication of this manuscript after addressing the minor comments listed below.

We thank the referee for this positive evaluation. We try to address all comments below. We would like to emphasize that some of the comments, although being of high relevance for the mission, go beyond the basic Level 2 algorithm development work supported by ESA and presented in this Special Issue. We are very much looking forward to working with the community on the validation and application of EarthCARE algorithms and products once the mission is in space, as well as on respective improvements of the methodologies later on.

1. Lines 35-45 and discussion of Figure 8. How much variation or uncertainty in aerosol size, absorption (SSA), asymmetry parameter, Angstrom exponent is associated within the aerosol classification for a particular set of lidar observables (lidar ratio, depolarization)? How does this uncertainty then impact the closure of TOA fluxes to the desired accuracy of 10 W/m²?

These questions go to the heart of the EarthCARE mission and belong to the radiation closure assessments to be done as a major science activity of EarthCARE. There is no simple answer to the questions. Variations/uncertainties in microphysical and optical aerosol properties do not translate one to one into changes of radiative properties and TOA fluxes. As can be seen from Fig. 8, in some cases the influence of variations will be low, while in other cases we have to deal with ambiguities and may need auxiliary information to reduce the errors in the radiative properties. Other points to be considered are the layering and/or mixing of aerosol types in an atmospheric column as well as the surface albedo or the presence of clouds below an aerosol layer. Furthermore, the instantaneous radiative effect strongly depends on the solar zenith angle.

Keeping all that in mind, we can use, e.g., the study of Kanitz et al. (2013) for some estimates. As shown in this paper, the same aerosol extinction profile leads to changes in the instantaneous TOA solar radiative effect of up to 10 Wm⁻² depending on the aerosol classification for a specific layer (in this case study for oceanic conditions, a lofted layer with an AOT of 0.2 of either dust, smoke, or a mixture of both above a marine boundary layer with an AOT of 0.2). Table 2 of the paper shows that a variation of asymmetry parameter or SSA of $\pm 5\%$ in one of the layers results in $\pm 5\text{--}10\text{ Wm}^{-2}$ in TOA solar aerosol radiative effect. Thus, we can conclude that a proper aerosol classification is essential for meeting the radiation closure goals of EarthCARE and that variations of microphysical properties within an aerosol class can be tolerated as long as they do not change the radiative properties by more than a few percent. Kanitz et al. (2013) also showed that the TOA radiative effect is smaller than the surface radiative effect, which could help in closure assessments that are supported/validated by more sensitive surface radiation measurements.

Overall, the questions of the referee can only be answered in detail by performing extended closure studies for a broad variety of scenarios, i.e., by comparing radiative transfer calculations based on

EarthCARE aerosol products with BBR measurements and by supporting such assessments with validation activities from ground.

We have added the additional reference and some discussion regarding the requirements in Sect. 2 (lines 74–78) and in Sect. 6.5 (discussion of Fig. 8, lines 519–521).

Reference:

Kanitz, T., Ansmann, A., Seifert, P., Engelmann, R., Kalisch, J., and Althausen, D.: Radiative effect of aerosols above the northern and southern Atlantic Ocean as determined from shipborne lidar observations, *J. Geophys. Res. Atmos.*, 118, 12,556–12,565, 2013.
<https://doi.org/10.1002/2013JD019750>

2. Lines 44 and 525 mention aerosol components associated with aerosol transport models (e.g. sulfate, organic carbon, black carbon). Line 525 mentions that these aerosol components in the CAMS model were mapped to the HETEAC components. How was this mapping done? It would be helpful to know this mapping in order to use the EarthCARE measurements to help evaluate the ability of aerosol transport models to apportion aerosol extinction and AOD to the model aerosol components.

The mapping between the HETEAC components and the CAMS types is presented in Qu et al.: “Numerical Model Generation of Test Frames for Pre-launch Studies of EarthCARE’s Retrieval Algorithms and Data Management System” (*Atmos. Meas. Tech. Discuss.*, <https://doi.org/10.5194/amt-2022-300>, 2022). It should be noted that this mapping was done in an ad hoc fashion with the limited aim of providing “realistic enough” test data and, though it may serve as a useful starting point, the mapping should likely be revisited for the purposes the reviewer has in mind. We added an additional hint to the reference in the text in Sect. 7.1 (line 540).

3. Line 166. Why were only ground-based observations of the lidar ratio and particle linear depolarization used without any airborne measurements?

So far, we used only measurements from networks and campaigns with strong involvement of TROPOS. In these cases, we have direct access to instruments and raw data as well as complete control over data evaluation and quality assurance, i.e., we are sure to follow always the same standards. We did not aim for completeness or high number of data points, but rather for a good representation of different aerosol types. Nevertheless, we see this work as a starting point and will open the collection for contributions from the community in the future. Please, see the paper by Floutsi et al.: “DeLiAn – a growing collection of depolarization ratio, lidar ratio and Ångström exponent for different aerosol types and mixtures from ground-based lidar observations” (*Atmos. Meas. Tech. Discuss.*, <https://doi.org/10.5194/amt-2022-306>, 2022) for a more detailed description of this work. – No changes made to the text.

4. Figure 2. It seems that the HETEAC fine strongly absorbing component provides an upper bound on the observed lidar ratio, the HETEAC coarse spherical component provides a lower bound on the observed lidar ratio, and both components provide lower bounds on the observed particle linear depolarization. However, there seems to be several observations of particle linear depolarization ratio that exceed the depolarization ratio of the HETEAC coarse non-spherical component. Could/should this component have been chosen such that its depolarization ratio was higher (~30%) to better bound the observed depolarization ratios?

At first glance, this is a very logical question. However, from the practical point of view, it is not advisable to follow this approach, which has to do with the natural variability of pure dust on the one hand and the limits of the scattering model for non-spherical particles on the other hand. While the corner points for the spherical particles follow naturally when realistic size and refractive-index parameters are applied in the Mie calculations, it is very tricky to obtain a physical meaningful model

representation for the dust particles, as discussed in Sect. 6.3.4 and shown in Fig. 5. Therefore, the dust component has been selected such that it stands for realistic (most appropriate) values of refractive index and particle size, and thus also for meaningful radiative properties. Otherwise, we would end up with a worse representation of dust in the model (always keeping in mind that the spheroidal shape model limits the physical representation anyhow).

In addition, one has to think about the consequences for the representation of pure dust and dust-containing mixtures. If we set the component further to the right (i.e., closer to 30 % depolarization), most of the pure dust observations, naturally occurring between 20 % and 30 % depolarization, would have to be represented in the model as a mixture of dust and non-dust particles, with consequences for the radiative properties. In contrast, with the approach of the probability distribution functions (PDFs) for the ATLID target classification (A-TC product, see Fig. 9), it is relatively easy to account for a wider range of natural dust cases by setting the PDF ellipse appropriately around the values defined for the dust component. In this way, best-estimate dust properties can be assigned to all observations that fall into the dust category with a certain probability.

Nevertheless, we also recommend that users adapt the parameters of the dust component as needed, when it is required for certain applications (e.g., regional studies). This can be done either in the model (by varying the refractive index, particle size, or shape) or in the application (e.g., in A-TC by shifting the PDFs). In any case, and in particular when optimal-estimation techniques are applied in retrievals, it is very important to assure a good overlap between the actual observation space (given by the variability in optical parameters, including measurement errors) and the chosen model space (determined by the variation of the microphysical parameters). – No changes made to the text.

5. Table 2. It would be helpful to know the values of lidar ratio, linear particle depolarization ratio, and Angstrom exponent corresponding to the standard Nd:YAG wavelengths (532, 1064 nm) used by many aerosol lidars including CALIOP.

These values (and also those for the MSI wavelengths) are included in the look-up table and provided in the associated Zenodo publication. Please refer also to our reply to comment 10 regarding the limitations of wavelength-dependent lidar-ratio calculations for non-spherical particles. We added a sentence with the reference in the text of Sect. 6.1 (lines 214–215). The reference is also provided at the end of the paper under *Data availability*.

Reference:

Wandinger, U., Floutsi, A. A., Baars, H., Haarig, M., Ansmann, A., Hünerbein, A., Docter, N., Donovan, D., van Zadelhoff, G.-J., Mason, S., and Cole, J.: HETEAC – The Hybrid End-To-End Aerosol Classification model for EarthCARE: Look-Up Table (LUT) for aerosol mixtures, 2023.
<https://doi.org/10.5281/zenodo.7732338>

6. Figure 4. Do the HETEAC component values of refractive index shown in Figure 4 correspond to dry (RH=0%?, RH<40%) conditions?

No. As can be seen in Fig. 4, the refractive index of the spherical coarse-mode particles follows the OPAC curve for sea salt at 70 % relative humidity (blue stars on the middle one of the three light-blue curves). For the weakly absorbing fine-mode particles, we chose the values of OPAC's water-soluble component at 50 % RH for the real part (red stars on the upper one of the three green curves), while for the imaginary part a constant low value of 0.001 was selected to allow for SSA values > 0.95 in the fine mode. We consider RH values of 70 % and 50 % as characteristic for marine and continental boundary layers, respectively. The assumption is supported by the fact that this modification of refractive-index values against the Aerosol_cci values leads to a much better agreement with the observations (location of the components in the $S-\delta$ diagram, cf. the lidar-ratio values for HETEAC and Aerosol_cci in Tables 4 and 5). No dependence on RH is considered for coarse non-spherical and absorbing fine-mode particles, which are assumed to have no strong water-uptake capability. All this

discussion is provided in Sect. 6.3 of the paper, where the selection of the values for the four components is justified in detail. – No changes made to the text.

7. Line 330. How accurate would RH have to be in order to be considered in HETEAC? Are there any plans to use model reanalysis RH fields when producing updated versions of the ATLID data products?

We plan to set up a project for studying RH effects on ATLID products, when validated spaceborne data will be available (in Phase E2 of the mission). Whether it makes sense to consider RH effects depends not only on the accuracy of the RH data, but also on the accuracy of the optical data and the ability to distinguish between mixing states and growth effects. Such investigations can only be done with real-world data, and they will need to be supported by respective ground-based/airborne validation efforts. We added a remark in Sect. 6.3.1 (lines 337-338) and a sentence at the end of Sect. 8.3 (lines 717-719).

8. Table 5. This table doesn't show dependence of linear particle depolarization on RH. Should we assume that depolarization for these particles is negligible for all RH?

Table 5 is for spherical coarse-mode particles, i.e., the depolarization is 0 by definition in all of the models presented in Table 5. If, in reality, we refer to sea salt instead of "coarse spherical particles", we know that depolarization occurs for low RH, as correctly outlined in the next comment. This effect, which is also connected to the consideration of RH information discussed above, is currently neglected in HETEAC. Respective discussion is provided in Sect. 8.2 (lines 668-677).

9. Line 400 and lines 705-712. The HETEAC components do not account for nonspherical sea salt. The conclusion mentions the presence of these aerosols in thin layers near the top of the marine BL (Haarig et al., 2017b) and gives the impression that these aerosols are not considered in the HETEAC scheme because: a) they are not observed often and only in thin layers near the BL top b) the depolarization ratio of these particles is relatively small (~8% at 355 nm), and c) ATLID may have insufficient resolution to detect these aerosols. An article was recently submitted to *Frontiers in Remote Sensing* that will indicate that items a), b), and perhaps c) are not necessarily true so the suggestion is made to begin considering how the HETEAC model would deal with such aerosols in the future.

We agree that more research is needed regarding this topic. Next to the paper by Haarig et al. (2017b), there is a study by Thomas et al. (2022) who used CALIPSO observations in the Southern Ocean and found that "for $RH < 60\%$, there are instances when the aerosol depolarization increases in the boundary layer". In their Fig. 9, they show that on average the depolarization in the marine boundary is higher for RH of 20–60 % than for RH of 60–90 % (see the discussion of this figure in the paper for more details). At the moment, we can only refer to the few available observations. We are looking forward to seeing the recently submitted study and, of course, we are open to include new findings in HETEAC. We added the additional reference and some more discussion in Sect. 8.2 (lines 668-677). Moreover, we clarified that the statements in Sect. 6.3.3 refer to humidity growth, i.e., wet conditions (lines 407-408).

Reference:

Thomas, M. A., Devasthale, A., and Kahnert, M.: Marine aerosol properties over the Southern Ocean in relation to the wintertime meteorological conditions, *Atmos. Chem. Phys.*, 22, 119–137, 2022. <https://doi.org/10.5194/acp-22-119-2022>

10. Lines 445-465. From this discussion, it seems that the HETEAC model for coarse, non-spherical aerosols (dust) can correctly reproduce the lidar observations of lidar ratio and linear depolarization

ratio at 355 nm but would be unable to do so at 532 nm? Is this correct? If so, how will this impact the use of the HETEAC scheme when relating ATLID observations of dust to those from CALIOP?

As shown in Fig. 6 and explained in the related text in Sect. 6.3.4, the major issue with the model is the spectral behavior of the backscatter coefficient, which shows large negative Angström exponents (of the order of -1 to -2) for realistic values of the refractive index (for a given size and shape distribution). This spectral slope of the backscatter coefficient leads to a large difference between the lidar ratios at 355 and 532 nm (of about a factor of 2), which is not supported by observations, even if negative Angström exponents (between 0 and -0.75) are often obtained. The following figure illustrates the situation in the S - δ diagram.

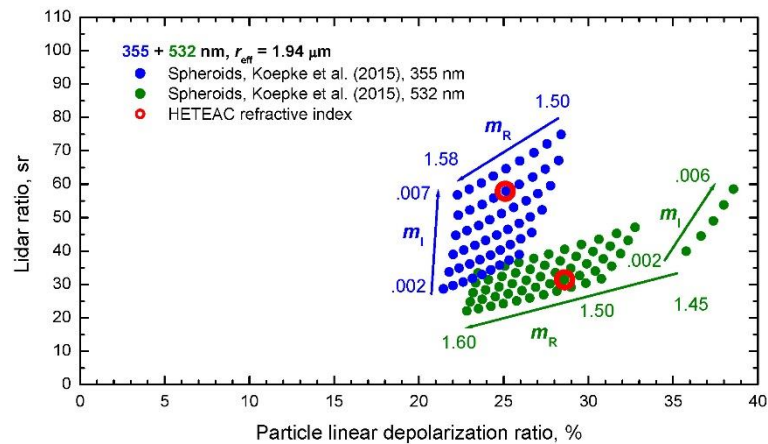


Figure 1: Simulated values of lidar ratio versus particle linear depolarization ratio at 355 nm (blue symbols) and 532 nm (green symbols) for the spheroid distribution after Koepke et al. (2015) with an effective radius of $1.94 \mu\text{m}$ and varying complex refractive index as indicated in the figure. The red circles indicate the HETEAC values.

Here, we can clearly see that for a given size and shape distribution, the lidar ratio at 532 nm is in general considerably smaller than at 355 nm. Even if it is known that the lidar ratio can differ from region to region due to the mineralogical composition of dust, observations show only slightly lower lidar ratios at 532 nm compared to 355 nm of less than 5 sr within a certain region (see Floutsi et al., 2022), what obviously cannot be reflected with the model (except we would reverse the absorption properties and assume low absorption in the blue and high absorption in the green, what is not realistic either). Regarding depolarization, the model correctly indicates higher values at 532 nm than at 355 nm.

As a consequence, when considering lidar observations at both wavelengths, e.g., to relate ATLID and CALIOP measurements or to develop multi-wavelength typing schemes, we cannot simply use the modelled values. Depending on the purpose, it is necessary to adjust the applied parameters with the help of observational values.

We want to emphasize here again that the issue with the spectral behavior of the backscatter coefficient is not just a problem for HETEAC. It is inherent in any retrieval that uses the spheroidal shape model to calculate lidar parameters from indirect observations (e.g., when inferring lidar ratios from Sun photometer measurements). Respective discussion is provided in Sect. 8.4. – No changes made to the text.

11. Figure 7. How does the HETEAC handle lidar observations of lidar ratio and/or particle depolarization that lie outside the triangles of points formed by the HETEAC components?

In principle, HETEAC does not handle lidar observations directly, but provides the baseline for different algorithms. These algorithms must consider the natural variability of aerosol properties and the measurement errors, but also invalid data. In case of the ATLID target classification (A-TC), as

shown in Fig. 9 and explained in the text, the parameter space is divided in six aerosol types. For each of the types, two-dimensional Gaussian PDFs are defined, which fill the entire parameter space. The PDFs assign a probability to each data point for belonging to a certain component or mixture. Similarly, HETEAC can be used to provide a priori information for optimal-estimation methods, which then deal with the variations of the observational data points within pre-defined error limits. In general, EarthCARE Level 2 algorithms apply various quality control mechanisms and flag the data accordingly. As can be seen in Fig. 10, A-TC contains an “out of parameter space” and a “missing data” class to deal with bad data. Thus, when the observation and its associated error places a data point too far from the triangle, the aerosol type is set to unknown. Respective thresholds and settings are configurable, as for all EarthCARE L2 algorithms. Explanations are provided in the context of Sect. 7.2.1; the statement in line 554 is clarified.

12. Figure 9 and Table 6 provide lidar observable values that correspond to the six tropospheric A-TC aerosol types and how these types are comprised of the HETEAC components. Lines 154-155 state that “The EarthCARE aerosol classification scheme shall preserve the aerosol types of CALIPSO as far as possible to allow long-term global investigations over the lifetime of both missions.” This is a commendable goal and will be very important as one would expect that researchers will attempt to combine the CALIOP and ATLID measurements for long term records. The six tropospheric A-TC aerosol types seem to coincide with some of the same aerosol types (at least in name) associated with the CALIOP tropospheric aerosol types. For these apparently common types, how do the lidar observables (at 532 nm) associated with the A-TC types coincide with the corresponding CALIOP values observed (particle depolarization) or assumed (lidar ratio) for these associated aerosol types? How do the underlying aerosol properties (e.g. size, SSA, refractive index) for this common aerosol types compare between A-TC and CALIOP aerosol types?

A harmonization of the long-term CALIPSO-EarthCARE data set for both aerosol and cloud observations (and subsequent radiation studies) is an ultimate goal and a challenging task for the atmospheric science community. We do not think that ad hoc approaches, such as a one-to-one relation of the aerosol types, are sufficient in this context, although common definitions of the targets provide already a good basis. For aerosols, we have to consider the wavelength conversion as well as the consequences of typing from either L1 (CALIOP) or L2 data (ATLID). While HETEAC and A-TC are built on intensive, i.e., concentration-independent, properties and do not consider (much) auxiliary information, the selection criteria in the CALIPSO typing scheme make use of the strength of the aerosol signal, the surface type, and the elevation of the layer (Omar et al., 2009; Kim et al., 2018). Therefore, we believe that a good harmonization of the data set will require some additional efforts, in particular the use of CALIPSO Level 2 data for a refinement of the typing as well as the development of type- and location-dependent conversion schemes.

The newest version of the CALIPSO typing scheme for the troposphere considers 7 subtypes, namely dust, marine, polluted continental/smoke, elevated smoke, clean continental, polluted dust, and dusty marine. Although we can relate the A-TC types to the rather similar CALIPSO subtypes (see Table 1 below), we cannot directly compare A-TC and CALIOP optical data. A-TC uses ATLID L2 particle depolarization ratio and lidar ratio at 355 nm together with configurable input parameters for the PDFs defining the types. The CALIOP algorithm applies an estimated particle depolarization ratio (L1 data product, 532 nm) and assumes an initial lidar ratio (at 532 and 1064 nm), which can be further adjusted within certain limits in the L2 retrievals (see Kim et al., 2018, Table 2). To compare the A-TC and CALIOP approaches, we can apply HETEAC to obtain 355-to-532-nm conversion information (the look-up table provides optical data for a variety of wavelengths and mixtures of the four components, <https://doi.org/10.5281/zenodo.7732338>). However, as mentioned above, care has to be taken for all mixtures containing non-spherical particles, because of the limitations of the spheroid model. For these cases, 355-to-532 nm conversions of the lidar ratio should be adjusted with the help of observations (e.g., by using DeLiAn, Floutsi et al., 2022). In Table 1 below, we relate the A-TC and CALIOP types and show comparisons of lidar ratios at 355 and 532 nm, including DeLiAn

values. When keeping the discussion above in mind, we find a very good agreement between the approaches/assumptions. This gives us confidence that we have a good starting point for harmonizing the long-term data set and we can build on it in future developments.

Regarding the comparison of the underlying microphysical and radiative properties, it seems that the aerosol microphysical model used in the development of the CALIOP typing scheme (Omar et al., 2009) is somewhat outdated. It was used to estimate the lidar ratios to be applied in the CALIOP retrievals at the beginning of the mission. Lidar ratios as well as aerosol types have been modified in the meantime (Kim et al. 2018) and, therefore, do not fully comply with the original model anymore. From the description of the model (Omar et al., 2009, Table 1), we do not directly get the information that is needed for comparisons with HETEAC (e.g., effective radius, SSA), i.e., further calculations are necessary. Oikawa et al. (2013, 2018) have used the model to estimate the global shortwave radiative forcing and present the SSA values that follow from the microphysical data (see their Table 1). However, they argue that “the SSA derived from the CALIOP aerosol models is not always realistic”. Compared to the HETEAC mixtures presented in Table 1 below, the SSA at 532 nm is the same for marine aerosol (0.99) and somewhat higher for dust (0.92 vs 0.90). For all other types, the SSA of the CALIOP model is lower than the one of HETEAC (e.g., 0.93 vs 0.97 for polluted continental and 0.83 vs 0.86 for smoke). Moreover, the effective radius (and thus the asymmetry parameter) following from the bimodal size distributions used in the CALIOP model is for some of the types quite unrealistic and not comparable with HETEAC. In particular, the dust type contains a large fraction of fine-mode particles leading to an effective radius of 0.4 μm (compared to 1.9 μm in HETEAC for the pure coarse mode or 1.2 μm for a mixture with 5 % fine-mode particles). The polluted dust model of CALIOP has nearly the same size distribution and effective radius as the pure dust model, i.e., the effective radius is also smaller than the one of the HETEAC dusty smoke mixture, which is about 0.7 μm . The largest particles of the CALIOP model occur in the clean continental background aerosol with an effective radius of 1.4 μm , while the polluted continental category shows the smallest value of 0.26 μm (comparable to the HETEAC continental pollution with 0.24 μm). From these findings, we conclude that the CALIOP model should be revisited, before it is used for any further studies. We also see how important radiation closure assessments and sub-orbital validation studies will be for the harmonization of the long-term data set, since in addition to the typing we need a good understanding of the aerosol microphysical properties to study aerosol radiative effects.

Table 1: Lidar ratio values (in sr) applied for ATLID and CALIOP (V4) aerosol typing

ATLID Type	A-TC 355 nm (adjustable)	HETEAC* 355 nm	HETEAC* 532 nm	DeLiAn 532 nm	CALIOP Type	Initial Value 532 nm
Marine	25	24 (5:0:90:5)	23 (5:0:90:5)	22 (Clean marine)	Clean marine	23
Dust	55	52 (0:0:5:95)	30 (0:0:5:95)	53 / 37 (Sahara / Asia)	Dust	44
Continental pollution	55	55 (50:5:40:5)	49 (50:5:40:5)	47 (Pollution)	Poll. cont. / smoke	70
				56 (Europ. bckgr.)	Clean cont.	53
Smoke	88	84 (30:50:10:10)	73 (30:50:10:10)	72 (Smoke)	Elevated smoke	70
Dusty Smoke	73	72 (5:10:5:80)	45 (0:10:0:90)	56 (Dust+smoke)	Polluted dust	55
Dusty Mix	43	45 (5:5:40:50)	34 (5:5:40:50)	32 (Dust+marine)	Dusty marine	37

*HETEAC values for selected volume mixing ratios as indicated
(weakly abs. fine : strongly abs. fine : spherical coarse : non-spherical coarse)

We added some discussion on the required future efforts in the conclusion and outlook section (lines 757-771, see also reply to comment 3 of Referee #1), but we do not go into the details discussed above, since harmonizing the CALIOP and ATLID data sets is a separate topic, which is beyond the scope of the paper. We will consider all these aspects in future publications.

References (for CALIOP SSA values, not used in the paper):

Oikawa, E., Nakajima, T., Inoue, T., and Winker, D.: A study of the shortwave direct aerosol forcing using ESSP/CALIPSO observation and GCM simulation, *Journal of Geophysical Research: Atmospheres*, 118, 3687–3708, 2013.
<https://doi.org/10.1002/jgrd.50227>

Oikawa, E., Nakajima, T., and Winker, D.: An evaluation of the shortwave direct aerosol radiative forcing using CALIOP and MODIS observations. *Journal of Geophysical Research: Atmospheres*, 123, 1211–1233, 2018.
<https://doi.org/10.1002/2017JD027247>

13. Figure 10. This is a nice figure to show an example of the HETEAC aerosol classification and brings to mind a few questions.

a. I don't recall seeing elsewhere in the paper a discussion of the spatial and vertical resolutions of the ATLID retrievals of lidar ratio and linear particle depolarization; what are these resolutions? Presumably the resolutions associated with the lidar ratio retrievals are coarser than the resolutions associated with the retrievals of particle linear depolarization. If this is true, how does the HETEAC classification deal with these different resolutions?

The sophisticated retrieval scheme is described in the respective paper on ATLID profile products by Donovan et al.: "The ATLID L2a profile processor (A-AER, A-EBD, A-TC and A-ICE products)", which will be submitted to the Special Issue soon. The algorithm works on a layer basis with different horizontal resolutions adapted to the specific scene. All products are provided at high (1 km), medium (e.g., 50 km), and low (150 km) horizontal resolution, and these three resolutions are always the same for all products (to make the products usable in combination). We added some text in Sect. 7.2.1 (lines 567-572, see also reply to comment 2 of Referee #1).

b. There are gaps (white areas) in the lidar ratio and depolarization images on the right. Are these gaps because the aerosol loading was too small for trustworthy measurements? If so, what are the minimum aerosol extinction values for which there will be expected retrievals of lidar ratio and linear particle depolarization? Likewise, what are the minimum aerosol extinction values required for the HETEAC aerosol classification?

In case of the depolarization the white gaps show regions for which the cross-polar channel showed a negligible signal with respect to the co-polar signal. White in this case therefore does not indicate no usable signal.

The white gaps in the lidar ratio can originate for two reasons. At first, the ATLID feature mask might have indicated that there are not enough co-polar Mie signals to indicate the existence of aerosol/ice cloud features. This will ensure that no retrieval is attempted. Secondly, the ATLID profile algorithm may not be able to perform a trustworthy retrieval.

Once there is a retrieval of lidar ratio and its error (and therefore the extinction), a target will be assigned. As mentioned above (see reply to comment 2 of Referee #1), it is expected that useful layer-average lidar-ratio retrievals (SNR of the retrieval better than 100 %) can be done for minimum extinction values on the order of $5.0e-6 \text{ m}^{-1}$ on the 50-100 km horizontal scale. We included this information in the additional text in Sect. 7.2.1 (lines 567-572, see also reply to comment 2 of Referee #1).

c. Looking again at the images on the right, there are more white areas (no retrievals?) associated with linear particle depolarization than for lidar ratio. Why? (I would have expected the opposite). Does the HETEAC algorithm still attempt to perform a classification if there is a retrieval of only one of two lidar observables?

The white areas correspond both to areas where the retrieved depolarization ratio is zero or below. The model-truth linear depolarization ratio for the aerosol in this scene is close to zero. Details can be found in the paper by Donovan et al.: “The Generation of EarthCARE L1 Test Data sets Using Atmospheric Model Data Sets” (Atmos. Meas. Tech. Discuss., <https://doi.org/10.5194/egusphere-2023-384>, 2023).

The aerosol classification procedure uses both the lidar ratio and the depolarization ratio along with their respective uncertainties. So, in principle, a retrieval of both observables is always technically available, however, one of the observables may have a very high error associated with it. In this case, the most-probable classification will still be selected. However, if the assessed probability is below a certain threshold, the classification will be set to “unknown”. – No changes made to the text.

d. The right side of the top right image shows relatively high values (70-80 sr) of the lidar ratio and low values of aerosol depolarization around 5 km. Figure 2a shows that these lidar ratios and depolarization ratios are associated are smoke and/or mixtures that contain smoke. However, the target classification shown in the bottom right seems to show this area is dominated by continental pollution with little, if any, smoke or smoke mixtures. Why?

After the retrieval of the target classification, a horizontal consistency check is performed using an ‘hybrid median’ type edge detection, gap filling procedure. This procedure uses the target type occurrence instead of the median as described in the AC-TC and A-PRO papers. This post-filtering will harmonize the types more than would be expected by the lidar ratio figure. More detail on this procedure can be found in Irbah et al.: “The classification of atmospheric hydrometeors and aerosols from the EarthCARE radar and lidar: the A-TC, C-TC and AC-TC products” (Atmos. Meas. Tech. Discuss., <https://doi.org/10.5194/egusphere-2022-1217>, 2022). – No changes made to the text.

14. Line 565. Can the column integrated aerosol classification probabilities be illustrated for the example shown in Figure 10?

Such a figure is provided in the paper on the ATLID layer products by Wandinger et al.: “Cloud top heights and aerosol layer properties from EarthCARE lidar observations: the A-CTH and A-ALD products”, which will be submitted to the Special Issue soon. We added a remark in the text (line 585-586).

15. Line 678. Suggest changing to “Ground-based and airborne measurements that measure...”

We added the airborne measurements in the sentence, now appearing in Sect. 8.1 (line 659).

Other changes not related to the referee comments

We changed the wording regarding the development of the experimental basis at the end of Sect. 4 to better describe our goals (lines 165-170).

We added the reference to the DeLiAn dataset:

Floutsi, A. A., et al.: DeLiAn – a growing collection of depolarization ratio, lidar ratio and Ångström exponent for different aerosol types and mixtures from ground-based lidar observations, 2023. <https://doi.org/10.5281/zenodo.7751752>

HETEAC – The Hybrid End-To-End Aerosol Classification model for EarthCARE

Ulla Wandinger¹, Athena Augusta Floutsis¹, Holger Baars¹, Moritz Haarig¹, Albert Ansmann¹, Anja Hünerbein¹, Nicole Docter², David Donovan³, Gerd-Jan van Zadelhoff³, Shannon Mason⁴, and Jason Cole⁵

¹Leibniz Institute for Tropospheric Research (TROPOS), Leipzig, Germany

²Free University of Berlin (FUB), Institute for Space Science, Berlin, Germany

³Royal Netherlands Meteorological Institute (KNMI), De Bilt, The Netherlands

⁴European Centre for Medium Range Weather Forecasts (ECMWF), Reading, United Kingdom

⁵Environment and Climate Change Canada (ECCC), Toronto, Ontario, Canada

Correspondence: Ulla Wandinger (ulla.wandinger@tropos.de)

Abstract.

The Hybrid End-To-End Aerosol Classification (HETEAC) model for the Earth Clouds, Aerosols and Radiation Explorer (EarthCARE) mission is introduced. The model serves as the common baseline for development, evaluation, and implementation of EarthCARE algorithms. It guarantees the consistency of different aerosol products from the multi-instrument platform and facilitates the conform specification of broad-band optical properties needed for EarthCARE radiative closure assessments. While the hybrid approach ensures that the theoretical description of aerosol microphysical properties is consistent with the optical properties of the measured aerosol types, the end-to-end model permits the uniform representation of aerosol types in terms of microphysical, optical, and radiative properties. Four basic aerosol components with prescribed microphysical properties are used to compose various natural and anthropogenic aerosols of the troposphere. The components contain weakly and strongly absorbing fine-mode as well as spherical and non-spherical coarse-mode particles and thus are representative for pollution, smoke, sea salt, and dust, respectively. Their microphysical properties are selected such that a good coverage of the observational phase space of intensive, i.e., concentration-independent, optical aerosol properties derived from EarthCARE measurements is obtained. Mixing rules to calculate optical and radiative properties of any aerosol blend composed of the four basic components are provided. Applications of HETEAC in the generation of test scenes, the development of retrieval algorithms for stand-alone and synergistic aerosol products from EarthCARE's Atmospheric Lidar (ATLID) and Multi-Spectral Imager (MSI), as well as for radiative closure assessments are introduced. Finally, [the implications of simplifying model assumptions and possible improvements are discussed](#) and conclusions for future [validation and](#) development work are drawn.

1 Introduction

The Earth Clouds, Aerosols and Radiation Explorer (EarthCARE) is a joint mission of the European Space Agency (ESA) and the Japan Aerospace Exploration Agency (JAXA) carrying four sensors, a cloud-profiling radar (CPR), a high-spectral-resolution cloud/aerosol lidar (ATLID), a cloud/aerosol multi-spectral imager (MSI), and a three-view broad-band radiometer

(BBR) (Illingworth et al., 2015; Wehr et al., 2023). Three instruments (ATLID, MSI, and BBR) provide information on the global aerosol distribution and contribute to the overarching EarthCARE goals of sensor synergy and radiation closure with respect to aerosols. The high-spectral-resolution lidar ATLID measures profiles of particle extinction and backscatter coefficients, lidar ratio, and particle linear depolarization ratio as well as aerosol optical thickness (AOT) at 355 nm along the track of the satellite (Donovan et al., 2023a). The MSI provides AOT at 670 nm (over land and ocean) and 865 nm (over ocean) across a 150 km wide swath (Docter et al., 2023). From combined ATLID and MSI data, the columnar Ångström exponent for the 355-670-865 nm spectral range can be inferred along track (Haarig et al., 2023). MSI observations are also used to extend the two-dimensional (2D) cross-sections from lidar and radar into the three-dimensional (3D) domain and thus allow respective 3D radiation modeling (Qu et al., 2022a; Cole et al., 2022). In this way, fluxes, heating rates, and radiances can be calculated and top-of-atmosphere (TOA) radiances and fluxes compared with those derived from BBR measurements (Barker et al., 2023). The EarthCARE aim is to obtain closure of measured and calculated TOA fluxes for a 100 km² snapshot view of the atmosphere with an accuracy of 10 Wm⁻², with the final goal to substantially decrease the uncertainties in our knowledge of global radiative forcing (Illingworth et al., 2015; Wehr et al., 2023).

The closure assessments require a proper aerosol classification based on the observations as well as an underlying aerosol model that connects microphysical, optical, and radiative properties of predefined aerosol types to derive the input parameters for radiative transfer calculations. Information on particle size (in terms of effective radius or asymmetry parameter) and on scattering and absorption properties over the relevant spectral range (in terms of wavelength-dependent complex refractive index or single-scattering albedo) is needed. Furthermore, the extinction profile measured with ATLID at 355 nm must be converted to the visible wavelength range by applying appropriate Ångström exponents, because typically the extinction at a wavelength of 500 to 550 nm is used as input for radiative transfer models. Aerosol classification from the spaceborne observations is also required for quantification of anthropogenic versus natural aerosol loadings of the atmosphere, investigation of aerosol-cloud interaction, as well as assimilation purposes and validation of atmospheric transport models, which carry components like dust, sea salt, smoke, and pollution. Finally, a well-defined aerosol classification model will enable an easier connection of EarthCARE to previous and upcoming space lidar missions and, in general, helps embed the mission into our understanding of scattering and absorbing aerosols in the climate system (see Li et al., 2022, for an overview).

To facilitate a common aerosol classification throughout the processing chain, and thus the consistency of all EarthCARE aerosol products including those from the radiative closure assessments, the Hybrid End-to-End Aerosol Classification (HETEAC) model has been developed. The model is based on a combined experimental and theoretical (i.e., hybrid) approach and allows the end-to-end simulation of aerosol properties, from microphysical to optical and radiative parameters of predefined aerosol types. The HETEAC concept was first introduced by Wandinger et al. (2016) and further developed since then. In this paper, we describe the basic considerations, developments, and current applications of HETEAC. The requirements for the EarthCARE aerosol classification scheme are summarized in Sect. 2. Section 3 discusses the idea of the hybrid end-to-end approach in more detail. Section 4 provides the context and heritage of the applied classification scheme. The experimental basis, on which the typing scheme is based, is briefly summarized in Sect. 5. Major results of the HETEAC model developments are presented in Sect. 6. Examples of the application of HETEAC in the development and implementation of the EarthCARE

processing chain are shown in Sect. 7. Further discussion [on the benefits and limitations of HETEAC](#) on implications of simplifying model assumptions and possible solutions to overcome limitations of the model is provided in Sect. 8. The paper closes with a conclusion and an outlook on [as well as plans for](#) further developments [provided](#) in Sect. 9.

60 2 Requirements for an EarthCARE aerosol classification scheme

The starting point for the development and implementation of an aerosol classification scheme for EarthCARE was the need to have a common tool that supports the instrument and data synergy and can be used as a baseline for algorithm development and evaluation across the development activities. In the operational phase of the mission, the approach should ensure the consistency of ATLID, MSI, and BBR Level 2a (L2a) and Level 2b (L2b) aerosol products throughout the processing chain
65 (Eisinger et al., 2023) as well as facilitate the consistent specification of broad-band aerosol optical properties necessary for radiative closure studies.

For the aerosol classification, a suitable set of basic aerosol types must be defined. This basic set should be complete enough to reasonably encompass the range of types encountered in nature, but it should not be more extensive than necessary to keep the number and kind of types traceable throughout different applications. The classification should allow for the separation
70 of natural and anthropogenic aerosols. The types need to be described consistently in terms of microphysical properties (size, shape, refractive index), which are used to represent them in scattering models, as well as in terms of optical and radiative properties, which are either observed with the EarthCARE instruments and used for the classification (lidar ratio, particle linear depolarization ratio, Ångström exponent) or applied in radiative transfer calculations and closure studies (single-scattering albedo, asymmetry parameter). [To achieve the goals of the EarthCARE mission regarding radiation closure, the aerosol classification must allow for assigning single-scattering albedo and asymmetry parameter with an accuracy of a few percent to each](#)
75 [aerosol layer in an atmospheric column. As shown by Kanitz et al. \(2013\), changes of \$\pm 5\%\$ in the radiative properties of a layer with medium AOT \(\$\sim 0.2\$ at 532 nm\) may lead to changes of \$\pm 5\text{--}10\text{ Wm}^{-2}\$ in the calculated instantaneous TOA solar aerosol radiative effect.](#)

The aerosol classification model must be compatible with the EarthCARE End-to-End Simulator (ECSIM, Donovan et al.,
80 2023b) as the major simulation and implementation test tool for the EarthCARE algorithms. It should provide input parameters for scene simulations with ECSIM and support ATLID, MSI, and BBR retrievals with required a priori information. Therefore, profile as well as columnar observations have to be considered. The model must be able to reproduce existing findings from ground-based and spaceborne observations and should be, as far as possible, consistent with previous approaches, in particular the one of the Cloud-Aerosol Lidar and Infrared Pathfinder Satellite Observations (CALIPSO, Omar et al., 2005, 2009; Kim
85 et al., 2018; Tackett et al., 2023), to facilitate long-term aerosol studies and trend analysis.

3 Hybrid end-to-end concept

The general concept of a hybrid end-to-end aerosol classification scheme is shown in Fig. 1. The red and blue colors stand for the hybrid approach. The aerosol modeling (red) starts from the theoretical description of microphysical particle properties for predefined aerosol types, from which the optical and radiative properties are calculated by applying appropriate scattering models. The measured optical data (from ATLID and MSI) are the starting point for the experimental part (blue). They are used for aerosol typing, from which microphysical and radiative particle properties follow via parametrization. The circle visualizes the end-to-end concept. The loop is closed by approaching the radiative properties from both sides. The connection to radiation measurements (from BBR) becomes possible by applying the retrieved parameters in radiative transfer calculations and comparing the modeled and measured values.

95 The concept shown in Fig. 1 works only, if the red and blue parts of the loop are interlinked. Aerosol typing and parametrization for the retrieval of microphysical and radiative properties from observed optical data are solely based on the underlying model. Therefore, the model must be designed such that the theoretical description of particle microphysics is consistent with experimentally derived optical properties and the observation space is well covered. In this way, a self-contained classification scheme is realized with the proposed hybrid, i.e., combined theoretical and experimental, approach.

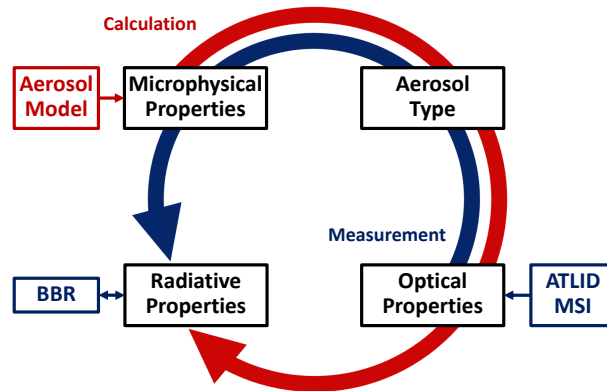


Figure 1. Hybrid end-to-end concept for aerosol classification.

100 While the hybrid end-to-end concept is a general approach, which can be used in various applications, HETEAC is specifically designed for the EarthCARE instrumentation. Table 1 lists the physical quantities used in the four aerosol property groups (see boxes on the circle in Fig. 1). In addition, their role in the EarthCARE retrieval chain is shown. The microphysical model considers particle size, shape, and spectral complex refractive index to allow the modeling of the optical and radiative properties from the ultraviolet (UV) to the far infrared (IR) spectral range as well as the proper coverage of the observation space.

105 The principles of aerosol typing via the definition of specific aerosol components and their mixtures are discussed in detail in the next sections. The optical properties measured by ATLID and MSI serve as input for the aerosol typing. The radiative prop-

erties and the Ångström exponent for the wavelength conversion from 355 to 500 or 550 nm follow from the parametrization according to the model.

Table 1. Aerosol property groups, relevant quantities covered in HETEAC, and their role in the EarthCARE retrieval chain.

Aerosol property group	Relevant quantities	Role in EarthCARE retrieval chain
Microphysical properties	Size distribution	Input for typing scheme
	Spectral complex refractive index	Input for scattering models
	Shape distribution	Input for radiation models
	(all per aerosol component)	Input for ECSIM
Aerosol type	Fraction of aerosol components	EarthCARE product
	(for pure and mixed types)	Output of typing scheme
		Input for MSI retrievals
Optical properties	Lidar ratio at 355 nm	EarthCARE products
	Particle linear depolarization ratio at 355 nm	Input for typing scheme
	Ångström exponent (355-670-865 nm, columnar)	
Radiative properties	Effective particle size or asymmetry parameter	Output of typing scheme
	Spectral single-scattering albedo	Input for radiation models
	Ångström exponent (355-500-550 nm)	Input for closure studies

4 Heritage of aerosol classification used for HETEAC

110 Prerequisite for any aerosol classification is the selection and definition of aerosol types that are to be identified from the measurements. Aerosol classification has a long history and different approaches are available from the literature. HETEAC developments make use of the heritage of previous attempts, but at the same time consider the specific needs of the EarthCARE mission.

115 One early effort to develop an aerosol classification model is the Optical Properties of Aerosols and Clouds (OPAC) database (Hess et al., 1998), which in turn builds on the earlier works of Shettle and Fenn (1979), Hänel and Zankl (1979), Deepak and Gerber (1983), D’Almeida et al. (1991), and Köpke et al. (1997). OPAC allows the construction of aerosol types from a number of basic aerosol components with well-defined microphysical properties under consideration of hygroscopic particle growth. Moreover, OPAC provides a comprehensive collection of refractive indexes of basic aerosol components over a wide wavelength range (0.25–40 μm). The new version OPAC 4.0 (Koepke et al., 2015) includes a non-spherical description of
120 dust particles and thus overcomes the previous shortcoming that the optical properties were solely based on Mie scattering calculations, i.e., only spherical particles could be treated. OPAC has been used in the development of HETEAC as source of refractive-index information and to study the influence of hygroscopic growth on particle optical properties.

A number of aerosol classification schemes rely on experimental findings from passive and active remote sensing and use specific optical fingerprints primarily based on intensive, i.e., concentration-independent, optical properties but also on aerosol load, geographic location, or altitude of occurrence. Such schemes have been developed in the context of the CALIPSO mission (Omar et al., 2005, 2009; Kim et al., 2018; Tackett et al., 2023), derived from dedicated lidar field studies (e.g., Burton et al., 2012; Groß et al., 2015) and network measurements (e.g., Nishizawa et al., 2017; Nicolae et al., 2018; Papagiannopoulos et al., 2018; Floutsi et al., 2022) or retrieved from passive remote-sensing observations (e.g., Russell et al., 2014; Hamill et al., 2016). Usually, these classification schemes distinguish three groups of aerosol types: 1) so-called pure types like marine, smoke, pollution, or dust aerosols, 2) mixtures of the former types, and 3) aerosol types that occur only in specific locations or under specific conditions like the polar regions or the stratosphere. A common understanding exists in defining the pure types of desert dust, marine aerosol, and anthropogenic pollution. These types can usually be well discriminated because of their well-defined and clearly different optical appearance. Biomass-burning aerosol or smoke is an important player as well, but it has a variable nature and is therefore treated differently. The optical and microphysical properties of smoke vary depending on the kind of burnt material (e.g., Savannah or boreal fires, crop burning), the kind of burning (smoldering or flaming), and the time and height of transport, i.e., the kind of atmospheric processing of particles. The classification schemes also use different ways to account for aerosol mixtures, e.g., mixtures of dust with biomass-burning, marine, or pollution aerosols or mixtures of marine and pollution aerosols.

Nowadays, advanced ground-based instrumentation provides a multitude of parameters from spectral and polarization-sensitive observations with active and passive sensors, which allows for a comprehensive aerosol classification under consideration of multiple aerosol types (e.g., Hamill et al., 2016; Nicolae et al., 2018; Floutsi et al., 2022). In contrast, spaceborne applications are still limited with respect to information content of the measurements. Therefore, more robust approaches based on less sophisticated but reasonable typing schemes are required. For instance, the aerosol project within the ESA Climate Change Initiative (Aerosol_cci) developed a model for passive satellite remote sensing based on four basic aerosol components (Holzer-Popp et al., 2013; de Leeuw et al., 2015). These components comprise two fine-particle modes – one strongly absorbing representing smoke and other soot-containing aerosols and one weakly absorbing describing typical anthropogenic emissions – and two coarse-particle modes – one with spherical particles characteristic for marine aerosol and one with non-spherical particles such as desert dust. Typical particle sizes and refractive indexes for the four modes were obtained from long-term ground-based Sun photometer observations in the framework of the Aerosol Robotic Network (AERONET, Holben et al., 1998).

For active remote sensing from space, standards have been set by the CALIPSO mission (Omar et al., 2005, 2009). Its version 4 aerosol classification scheme (Kim et al., 2018) considers seven aerosol (sub-)types for the troposphere (marine, clean continental, polluted continental/smoke, desert dust, polluted dust, dusty marine, and elevated smoke). For the stratosphere, the recent update to version 4.5 (Tackett et al., 2023) includes polar stratospheric aerosol, volcanic ash, sulfate, smoke, and unclassified aerosol. CALIPSO aerosol typing relies on lidar Level 1 data, since the methodology has been developed primarily to select proper lidar ratios for Level 2 data retrievals. Thus, selection criteria comprise integrated attenuated backscatter, esti-

mated particle depolarization ratio, and vertical location of the layer as well as the kind of surface above which the observation was made.

The EarthCARE aerosol classification scheme shall preserve the aerosol types of CALIPSO as far as possible to allow long-term global investigations over the lifetime of both missions. However, a more robust typing based on Level 2 data is applied. Thanks to the high-spectral-resolution lidar approach, ATLID retrievals do not require an a priori estimate of the particle lidar ratio, but provide this quantity together with the particle linear depolarization ratio as an observable. EarthCARE's aerosol-type product can thus rely on measured intensive, i.e., concentration-independent, particle properties. For the theoretical description of the microphysical particle properties as part of the hybrid end-to-end concept, the Aerosol_cci approach of using four basic aerosol components has been adopted and modified according to the requirements discussed in Sect. 2. ~~An experimental basis has been established (Floutsi et al., 2022, 2023) to support the aerosol typing at the ATLID wavelength of 355 nm as well as the conversion of results from the UV to the visible (VIS) and near-IR spectral range to harmonize EarthCARE and CALIPSO observations (at 532 and 1064 nm) later on. Since ATLID observations are performed at 355 nm and shall be harmonized with the CALIPSO observations at 532 and 1064 nm, an experimental basis for aerosol typing at the ATLID wavelength and the conversion of results from the UV to the visible (VIS) and near-IR spectral range has been established.~~ The experimental basis and its use in the development of HETEAC is briefly summarized in the next section.

5 Experimental basis for aerosol typing

Figure 2 shows a collection of ground-based tropospheric observations of lidar ratio S and particle linear depolarization ratio δ at 355 nm as well as extinction-related Ångström exponent $\hat{a}_{\text{ext,UV-VIS}}$ for the 355-to-532 nm wavelength pair. The measurements were taken at various locations in the northern and southern hemisphere between 2006 and 2021. They include contributions from the European Aerosol Research Lidar Network (EARLINET; Pappalardo et al., 2014), PollyNET – the network of lidar systems of type Polly^{XT} operated by the Leibniz Institute for Tropospheric Research (TROPOS), including mobile systems operated on research vessels (Engelmann et al., 2016; Baars et al., 2016) –, and various field campaigns, in which TROPOS participated over the past 16 years. An early version of the data collection, which served as the starting point for the HETEAC development, was presented in Illingworth et al. (2015). A detailed description of the extended experimental basis is provided by Floutsi et al. (2022, 2023).

The symbols in Fig. 2 are color-coded to distinguish major aerosol types and their mixtures. Orange symbols show observations of dust in different regions of the world, from the Caribbean to Central Asia (e.g., Tesche et al., 2009a; Groß et al., 2011; Haarig et al., 2017a; Hofer et al., 2020). Blue dots indicate measurements in clean marine environments, obtained at Cabo Verde and during cruises with German research vessels across the Atlantic (Groß et al., 2011; Rittmeister et al., 2017; Bohlmann et al., 2018). Black dots represent observations of fresh biomass-burning smoke, most of them taken close to fire spots in the Amazon Rain Forest (Baars et al., 2012) and in South Africa (Giannakaki et al., 2015). Aged biomass-burning smoke, measured after long-range intercontinental transport, is indicated by green squares with black edges (e.g., Haarig et al., 2018). Red symbols stand for pollution (dots) and continental background aerosols (open circles) (e.g., Giannakaki et al.,

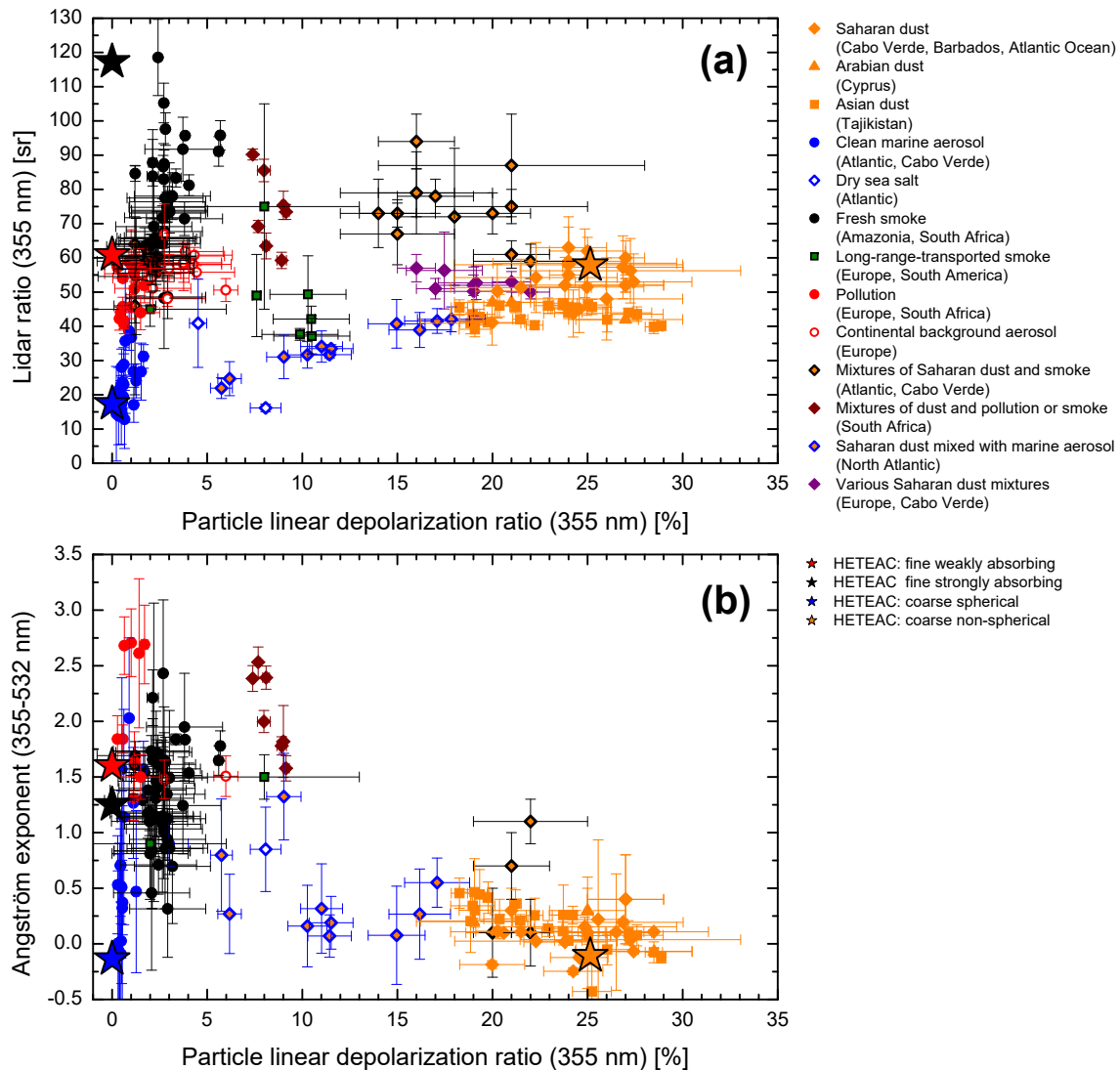


Figure 2. Experimental values of (a) lidar ratio and (b) extinction-related Ångström exponent for the 355-to-532 nm wavelength pair versus particle linear depolarization ratio at 355 nm for the troposphere. The symbols indicate individual layer-mean values from selected world-wide measurements with multiwavelength Raman polarization lidars in EARLINET, PollyNET, and during various field campaigns as indicated in the legend to the right of panel (a). The stars show the respective values of the four aerosol components defined in HETEAC, see legend to the right of panel (b).

190 2015). Different mixtures of these major types such as dust mixed with marine aerosol (e.g., Rittmeister et al., 2017; Bohlmann et al., 2018), pollution, or smoke (e.g., Tesche et al., 2009b; Groß et al., 2011; Kanitz et al., 2014; Giannakaki et al., 2015) are also represented. A complete list of campaigns and references is given in Table 2 of Floutsis et al. (2022). It should be noted that

the number of data points in the two panels of Fig. 2 is different, because extinction data at 532 nm to calculate the Ångström exponent were not always available.

195 From the experimental basis, it can be seen that the discrimination power for the major aerosol types is high in the S - δ space (see Fig. 2a), i.e., the intensive optical properties available from ATLID are well suited for aerosol classification. While the particle linear depolarization ratio allows the identification of dust and dust-containing aerosol mixtures, the lidar ratio is especially useful to distinguish between small absorbing and large non-absorbing spherical particles. Knowledge of the Ångström exponent (see Fig. 2b), which will be available for the atmospheric column by combining ATLID and MSI data, can
200 be helpful for aerosol typing as well, but only in combination with additional parameters, since otherwise the ambiguities are very high.

Fig. 2 also shows the theoretical values for the basic aerosol components defined in HETEAC. They are marked with stars of different color, which relates them to the major aerosol types found from the observations. In the next section, the definition of these basic aerosol components is explained.

205 6 HETEAC model

6.1 Definition of basic aerosol components

HETEAC uses four predefined aerosol components to simulate tropospheric aerosol. Similar to the approach of Aerosol_cci, they comprise two fine-particle and two coarse-particle modes. The two fine modes consist of either weakly or strongly absorbing spherical particles. One coarse mode contains non-absorbing spherical particles, while the second one is made up of
210 non-spherical particles with wavelength-dependent absorption. The four modes can be interpreted, in an idealized manner, to represent pollution (fine, spherical, weakly absorbing), fresh smoke (fine, spherical, strongly absorbing), marine particles (coarse, spherical, non-absorbing), and dust (coarse, non-spherical, absorbing). More realistic aerosol types can be modeled by mixing these four components. The microphysical properties of the four components and the resulting optical parameters of interest are summarized in Table 2. [More information, e.g., on the optical parameters at other wavelengths, can be found in the](#)
215 [associated data publication \(Wandinger et al., 2023a\)](#). In the following, a detailed description of the modeling and the selection of the physical parameters for each mode is provided.

6.2 Modeling of microphysical properties

A consistent end-to-end aerosol modeling requires the consideration of

- particle size,
- 220 – particle shape, and
- complex refractive index.

Table 2. Properties of the four predefined aerosol components in HETEAC (r_{eff} – effective radius, $r_{0,N}$ – mode radius of the number size distribution, $r_{0,V}$ – mode radius of the volume size distribution, $\ln \sigma^*$ – logarithmic mode width, m_R – real part of the refractive index, m_I – imaginary part of the refractive index, S – lidar ratio, δ – particle linear depolarization ratio, $\hat{a}_{\text{ext,UV-VIS}}$ – extinction-related 355-to-532 nm Ångström exponent).

Property	Fine mode	Fine mode	Coarse mode	Coarse mode
	weakly absorbing	strongly absorbing	spherical	non-spherical
$r_{\text{eff}}, \mu\text{m}$	0.14	0.14	1.94	1.94
$r_{0,N}, \mu\text{m}$	0.07	0.07	0.788	0.788
$r_{0,V}, \mu\text{m}$	0.1626	0.1626	2.32	2.32
$\ln \sigma^*$	0.53	0.53	0.6	0.6
m_R (355 nm)	1.45	1.50	1.37	1.54
m_I (355 nm)	0.001	0.043	4e–8	0.006
Shape	spherical	spherical	spherical	spheroid
S (355 nm), sr	60.9	117.3	17.4	57.9
δ (355 nm), %	0.0	0.0	0.0	25.1
$\hat{a}_{\text{ext,UV-VIS}}$	1.60	1.25	–0.14	–0.11

In HETEAC, each aerosol component is defined by a mono-modal log-normal size distribution of either spherical or spheroid particles and a wavelength-dependent complex refractive index, which is constant for all particle sizes within the mode.

6.2.1 Particle size distribution

225 The log-normal particle size distribution can be described mathematically in different ways. We provide a brief summary, which is helpful to quickly compare the parameters used in different models and tools and to prove their consistency in the EarthCARE processing chain. Two common equations to describe the size distribution are:

$$n(r) = \frac{dN(r)}{dr} = \frac{N}{\sqrt{2\pi}r\sigma} \exp\left(-\frac{[\ln(r/r_{0,N})]^2}{2\sigma^2}\right), \quad (1)$$

$$230 \quad n(r) = \frac{dN(r)}{dr} = \frac{N}{\sqrt{2\pi}r \log \sigma^* \ln 10} \exp\left[-\frac{1}{2} \left(\frac{\log(r/r_{0,N})}{\log \sigma^*}\right)^2\right]. \quad (2)$$

These equations, which describe the particle number concentration n as a function of particle radius r (with the total particle number N) are completely consistent, but may cause confusion due to the somewhat different description of the mode width (also called shape parameter of the size distribution). The relation between the logarithmic mode width σ (variance) in Eq. (1) and the mode width σ^* (geometric standard deviation) in Eq. (2) is $\sigma = \ln \sigma^*$. It should be noted that some authors use Eq. (1),
235 but write $\ln \sigma$ instead of σ . In this case, σ indicates the geometric standard deviation and $\ln \sigma$ is the variance. Therefore, the meaning of σ must be carefully checked when different aerosol models are compared.

The mode radius $r_{0,N}$ is related to the effective radius r_{eff} of a mono-modal size distribution by

$$r_{\text{eff}} = r_{0,N} \exp(2.5\sigma^2). \quad (3)$$

240 Instead of the number size distribution, often the volume size distribution $v(r)$ is applied, i.e., in Eq. (1) and (2) N is replaced by V , and the mode radius $r_{0,V}$ of the volume size distribution is used, which is calculated from $r_{0,N}$ as

$$r_{0,V} = r_{0,N} 10^{3 \log^2(\sigma^*) \ln 10} = r_{0,N} 10^{3\sigma^2 / \ln 10}. \quad (4)$$

Furthermore, a logarithmic representation is commonly used and thus the size distribution is given as

$$\begin{aligned} \frac{dV(r)}{d \ln r} &= \frac{V}{\sqrt{2\pi}\sigma} \exp\left(-\frac{[\ln(r/r_{0,V})]^2}{2\sigma^2}\right) \\ &= v(r) \frac{dN(r)}{d \ln r} = v(r) r \frac{dN(r)}{dr} = v(r) \frac{N}{\sqrt{2\pi}\sigma} \exp\left(-\frac{[\ln(r/r_{0,N})]^2}{2\sigma^2}\right). \end{aligned} \quad (5)$$

245 ECSIM programming is based on Eq. (1), whereas the OPAC model uses Eq. (2). AERONET retrievals as well as the spheroid model of Dubovik et al. (2006), which is used below, provide the size distribution in terms of Eq. (5). ECSIM uses the effective radius r_{eff} and the variance σ as input parameters to describe a mono-modal size distribution and then internally calculates the radius $r_{0,N}$ from the effective radius after Eq. (3).

6.2.2 Particle shape distribution

250 For the calculation of polarization-dependent scattering properties, a non-spherical particle shape model together with the respective scattering code is needed. Light scattering by non-spherical particles is a complex topic covered by a wide field of research. In recent years, many efforts have been made to realistically model the shapes of atmospheric particles and calculate their scattering properties (e.g., Gasteiger et al., 2011; Kemppinen et al., 2015; Bi et al., 2018; Saito and Yang, 2021). However, these models are still limited, in particular regarding the maximum particle size, and usually require high computational efforts, 255 which makes them difficult to apply for our purpose. Therefore, as an initial approach for the HETEAC parametrization, we use the traditional way of approximating non-spherical particles by spheroids, i.e., prolates and oblates with a predefined distribution of axis ratios. The axis ratio is defined as the ratio of the length of the axis of rotational symmetry to the length of the axis perpendicular to it, i.e., the axis ratio of prolates is larger than 1 and the one of oblates is less than 1.

Dubovik et al. (2006) provided a pragmatic solution in the form of a spheroid model based on look-up tables (LUTs) of 260 precalculated size- and shape-dependent optical properties of randomly oriented particles. The LUTs cover 25 bins of axis ratios between 0.33 and 3, 41 bins of size parameters between 0.012 and 625 (on a logarithmic-equidistant scale), 22 bins of the real part (1.29–1.7) and 16 bins of the imaginary part (1×10^{-10} –0.5) of the refractive index, and 181 scattering angles from 0° to 180° . The model allows the simulation of properties of shape mixtures. The large size range is realized by combining the advanced T-matrix code (Mishchenko and Travis, 1998; Mishchenko et al., 2002) for size parameters up to about 30 with the 265 approximate geometric-optics–integral-equation method (Yang and Liou, 1996) for larger sizes. Dubovik et al. (2006) propose

one specific mixture of spheroids that well reproduces the scattering properties of dust measured in the laboratory. Customized mixtures or individual shapes can be used in the model as well. In addition, it is possible to mix spherical and non-spherical particles.

The spheroid model is applied to calculate optical properties of aerosol types containing non-spherical particles in HETEAC. Because the model is very fast, it can be used to study a large variety of parameter combinations and to select appropriate ones.

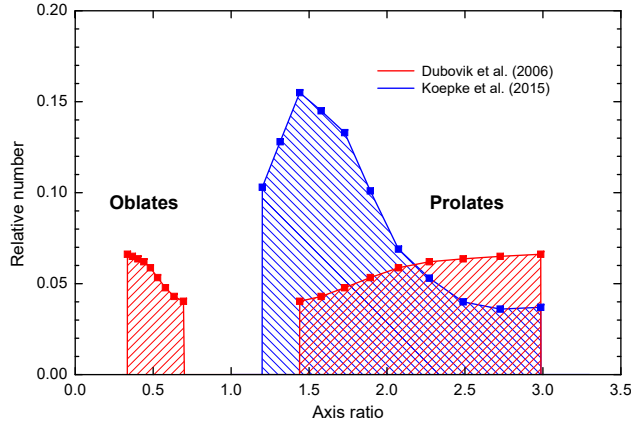


Figure 3. Axis ratio distribution proposed by Dubovik et al. (2006), shown in red, and Koepke et al. (2015), shown in blue. The latter one is interpolated from the original linear to the logarithmic grid needed for calculations with Dubovik’s code for spheroid scatterers. The logarithmic grid is indicated by the symbols.

Regarding the shape distribution, there are two proposals available from the literature, one by Dubovik et al. (2006), which is implemented in various retrieval approaches (e.g., in Aerosol_cci), and one by Koepke et al. (2015), which is used in OPAC 4.0. Whereas the first one is a more or less arbitrary assumption, the latter one follows experimental observations by Kandler et al. (2009) and has already been used to produce the scattering libraries for dust in earlier versions of ECSIM. Figure 3 shows the axis-ratio distributions of the two models. Dubovik’s distribution is given for logarithmic-equidistant intervals as used in the spheroid scattering code. The shape distribution of oblates and prolates is symmetric on the logarithmic scale. The distribution used in OPAC 4.0 is provided on a linear scale, but has been interpolated to the logarithmic scale here to make it useable for calculations with Dubovik’s code. A discussion of results obtained for these shape distributions is provided in Sect. 6.3.4.

In the context of the shape discussion, it should be noted that the definitions regarding the particle size distribution in Sect. 6.2.1 are based on the particle radius and thus strictly hold for spherical particles only. The size of non-spherical particles is usually described via an equivalent radius (or diameter). Depending on application, equivalence with respect to a sphere of the same volume, surface area, or geometrical cross section is used, i.e., a volume-equivalent (r_{ve}), surface-area-equivalent (r_{se}), or cross-section-equivalent radius (r_{ce}) is defined. For randomly oriented convex bodies, the ratio of surface area to average cross section is constant and equal to four (Cauchy’s theorem on convex bodies). Thus, $r_{se}/r_{ce} = 1$ as long as we restrict our calculations to spheroids. The ratio of surface area to volume increases with increasing aspect ratio (ratio of major to minor axis) of the spheroid, i.e., $r_{se}/r_{ve} > 1$. Thus, the definition of particle size via parameters like effective radius or size parameter

becomes ambiguous and relations between, e.g., surface-area and volume size distributions developed for spheres do not hold anymore. However, in the case of spheroids with axis ratios between 0.33 and 3, as used here, $r_{se}/r_{ve} < 1.1$. Therefore, in a first approximation, shape effects in the definition of size distribution parameters may be neglected. Nevertheless, one should keep in mind that, e.g., the true effective radius of an ensemble of non-spherical particles is larger (typically 5–10 % for spheroids) than the one given for an ensemble of volume-equivalent spheres.

6.2.3 Spectral complex refractive index

The real and imaginary parts of the complex refractive index describe the particles' ability to scatter and absorb electromagnetic radiation, respectively. Strictly speaking, the refractive index is a wavelength-dependent property of a certain material. Particles may be composed of different materials (e.g., dust particles are made up of different minerals), and an ensemble of particles in an atmospheric aerosol probe typically consists of particles with different composition. For the purpose of aerosol modeling, usually a common (average) refractive index is assumed for all particles of an ensemble. In our case, a wavelength-dependent complex refractive index is assigned to each of the four basic aerosol components.

Figure 4 shows the spectral complex refractive in the wavelength range from 300 to 2250 nm as used for different aerosol components in the OPAC and Aerosol_cci models (Hess et al., 1998; Holzer-Popp et al., 2013). In addition, various measurements of dust refractive indexes in the UV to near-IR range are shown (Kandler et al., 2009; Müller et al., 2009; Petzold et al., 2009; Di Biagio et al., 2019). The values recommended for the four HETEAC components at the ATLID and MSI measurement wavelengths and at 550 nm are indicated with stars. They are also listed in Table 3. Further discussion and analysis of the selected values is provided for each basic component in Sect. 6.3.

No investigations for wavelengths larger than 2250 nm have been performed in the context of HETEAC developments so far. As mentioned above, the OPAC database provides refractive-index values up to 40 μm wavelength, which can be used for broad-band radiative transfer calculations. However, updates similar to the ones performed for the short wavelengths (see discussion below) should be envisaged in view of recent findings, e.g., for dust, as recommended by Di Biagio et al. (2017).

Table 3. Complex refractive index of the four predefined aerosol components at selected wavelengths.

Wavelength	Fine mode weakly absorbing	Fine mode strongly absorbing	Coarse mode spherical	Coarse mode non-spherical
355 nm	$1.450 - 0.001i$	$1.50 - 0.043i$	$1.370 - 4.0 \times 10^{-8}i$	$1.54 - 6.0 \times 10^{-3}i$
550 nm	$1.440 - 0.001i$	$1.50 - 0.043i$	$1.360 - 4.0 \times 10^{-9}i$	$1.53 - 3.0 \times 10^{-3}i$
670 nm	$1.435 - 0.001i$	$1.50 - 0.043i$	$1.358 - 4.0 \times 10^{-8}i$	$1.53 - 8.0 \times 10^{-4}i$
865 nm	$1.430 - 0.001i$	$1.50 - 0.043i$	$1.354 - 3.0 \times 10^{-6}i$	$1.53 - 5.0 \times 10^{-4}i$
1650 nm	$1.405 - 0.001i$	$1.50 - 0.043i$	$1.340 - 2.4 \times 10^{-4}i$	$1.53 - 5.0 \times 10^{-4}i$
2210 nm	$1.360 - 0.001i$	$1.50 - 0.043i$	$1.310 - 1.5 \times 10^{-3}i$	$1.53 - 5.0 \times 10^{-4}i$

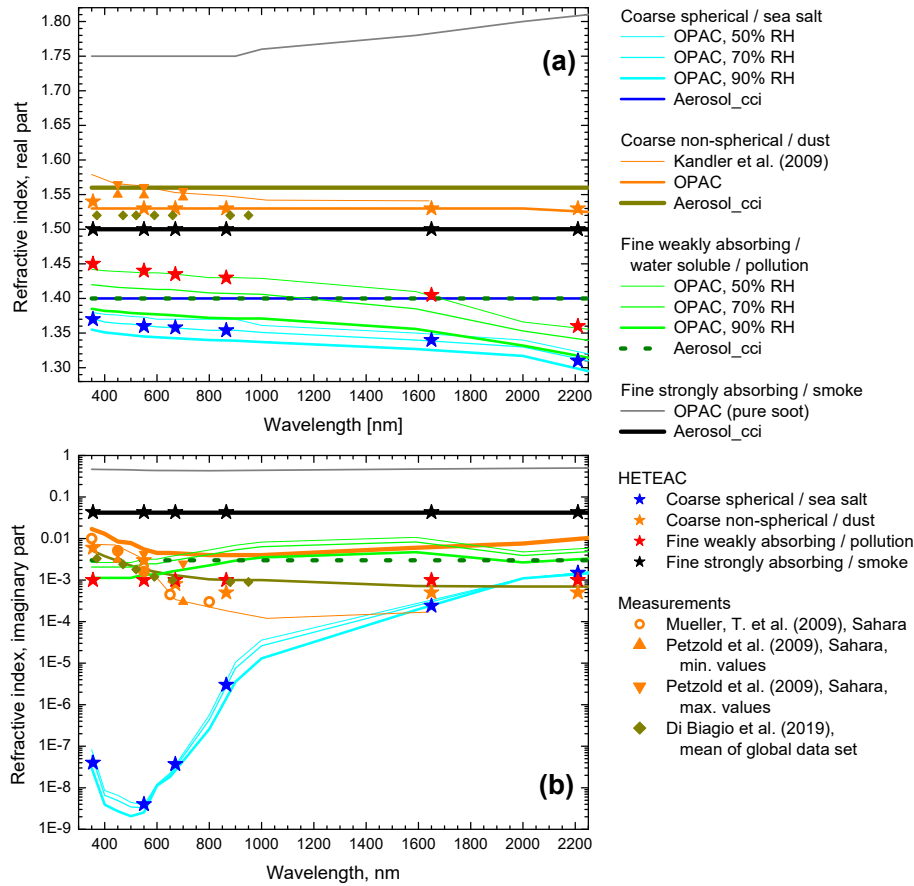


Figure 4. Real (a) and imaginary part (b) of the spectral refractive index from different models and measurements. The stars indicate the values selected for HETEAC.

6.3 Selection of microphysical parameters for the basic aerosol components

310 The microphysical properties of the four basic aerosol components have been selected starting from the available knowledge in the literature, as already indicated in Sect. 6.2. The fine-tuning of the parameters was done by comparing the resulting optical parameters with the experimental basis presented in Sect. 5. As mentioned in Sect. 6.1, the four basic components are considered to mainly represent anthropogenic pollution (small, weakly absorbing particles), fresh biomass-burning aerosol (small, strongly absorbing particles), marine aerosol (large spherical, non-absorbing particles), and mineral dust (large non-
 315 spherical, moderately absorbing particles). In the following, the criteria applied in the selection of the microphysical parameters and the consequences regarding the representation of real-world aerosols are discussed. [The reader is also referred to Sect. 8, where further implications of the concept are described.](#)

6.3.1 Weakly absorbing fine-mode particles

Fine particulate matter is either directly emitted or generated from precursors by gas-to-particle conversion. Major anthropogenic sources are the combustion of fossil and bio fuels for industrial, transportation, and heating purposes as well as agricultural activities. Anthropogenic aerosol is often modeled as a mixture of water-soluble, i.e., hygroscopic, and insoluble material. The absorption properties can be determined, e.g., via the fraction of insoluble soot contained in the mixture. Compared to smoke from biomass burning (see next paragraph), anthropogenic aerosol is assumed to be weakly to moderately absorbing. Typing schemes use names like continental pollution, industrial pollution, or urban aerosol for the classification of anthropogenic aerosol and sometimes introduce sub-types to distinguish emissions from different sources or regions with different optical properties (e.g., Russell et al., 2014).

For weakly absorbing fine-mode particles in HETEAC, the size distribution from the Aerosol_cci model is adopted (see Table 2), but the refractive index is modified. Aerosol_cci uses a constant value of $m = 1.40 - 0.003i$ (see Fig. 4, dashed olive lines). In HETEAC, the real part has a slight spectral slope following the OPAC simulations for water-soluble particles at 50 % relative humidity (see red stars and thin green line in Fig. 4a). A constant imaginary part of $m_i = 0.001$ is chosen, i.e., the absorption is reduced compared to the respective component of the Aerosol_cci model. In this way, a better coverage of the observation space is realized. For instance, the lidar ratio at 355 nm is 78 sr when using the Aerosol_cci refractive index, which obviously is too high to properly describe the optical properties of polluted continental aerosol (see Fig. 2). The modified value in HETEAC leads to a more realistic value of 61 sr. If needed, the fine-mode absorption can be increased by mixing of the weakly absorbing with the strongly absorbing component, which has the same size distribution (see next paragraph and Sect. 6.4).

Next to absorption, also the size of the particles can change, in particular in dependence on relative humidity (see also Sect. 8.3). Because accurate enough humidity information to describe hygroscopic particle growth is usually not available for spaceborne retrievals, the effect is not explicitly considered in HETEAC. To study its potential impact on the retrievals, the change of optical properties in dependence on hygroscopic growth has been investigated with OPAC.

Table 4 compares the optical properties obtained with HETEAC and the Aerosol_cci model for weakly absorbing fine-mode particles with two representations of continental pollution provided by OPAC. In OPAC, water-soluble (*waso*), insoluble (*inso*), and soot components (*soot*) are mixed to represent various continental aerosol conditions. Whereas the water-soluble and soot modes have small mode radii ($r_{0,N} < 0.05 \mu\text{m}$, $r_{\text{eff}} < 0.27 \mu\text{m}$), the insoluble particle mode contains large particles ($r_{0,N} = 0.47 \mu\text{m}$, $r_{\text{eff}} = 3.9 \mu\text{m}$) to account also for (a small fraction of) soil dust and organic or biogenic material in the continental aerosol. The latter fraction has been omitted in the second case of OPAC simulations (urban) shown in Table 4. It can be seen that the water-soluble component leads to an increase of the effective radius and to slightly varying optical properties in dependence on relative humidity due to hygroscopic growth. However, the lidar ratio always remains in a range of about 60–70 sr, i.e., its sensitivity is low and the value of 61 sr resulting from the microphysical parameters chosen for HETEAC is a good representation for anthropogenic aerosol independent of actual relative humidity. In addition, it should

be noted that Zieger et al. (2013) found that OPAC tends to overestimate the humidity-growth effects for humidity values of 50–80 %, i.e., the change in optical data for moderate relative humidity may be even smaller than shown in Table 4.

Ångström exponents obtained with HETEAC and the Aerosol_cci model are higher than those calculated with OPAC (see Table 4). The UV-VIS wavelength pairs used in the simulations are 355 and 532 nm for HETEAC and Aerosol_cci and 350 and 500 nm for OPAC. For VIS-IR, the pairs are 532 and 865 nm and 500 and 800 nm, respectively. Values of about 1.6 in the UV-VIS and 2.2 in the VIS-IR wavelength range are found for the weakly absorbing fine-mode particles in HETEAC and the Aerosol_cci model, in good agreement with experimental results. OPAC gives Ångström exponents between 1.0 and 1.2 in the UV-VIS and between 1.3 and 1.5 in the VIS-IR range for a relative humidity between 50 and 95 %, which are obviously too low to well represent polluted conditions. The relatively low values for moderate humidity do also not increase significantly, when the coarse insoluble particles are completely dropped in the simulations (see Table 4). The reason for the low Ångström exponents lies in the wider size distribution of the fine-mode particles used in OPAC ($\sigma^* = 2.24$ instead of 1.82 for HETEAC and Aerosol_cci). Thus, for the same effective radius, more optically active large particles on the right wing of the size spectrum contribute to the scattering properties, without a compensation from the very small and optically inefficient particles on the left wing. It can be concluded that the size-distribution parameters chosen for the fine mode in HETEAC, by following Aerosol_cci and thus climatological values from AERONET, provide a better representation of natural conditions than OPAC.

6.3.2 Strongly absorbing fine-mode particles

As already discussed in Sect. 4, smoke from biomass burning is of variable nature. Its microphysical and optical properties depend on the generation processes (burnt material and kind of fire) as well as on processes during transport in the atmosphere. Smoke is often detected in pronounced lofted atmospheric layers, which can travel over very long distances and remain in the atmosphere for days to weeks. Such smoke plumes may contain not only burnt material but also other aerosols like soil dust taken up during the fire event. Therefore, the modeling of smoke properties is challenging, and mixtures of different components should be taken into account for a realistic representation. Nevertheless, freshly emitted smoke particles are of sub-micron size and contain a high fraction of soot and other absorbing materials, i.e., an absorbing fine mode is required for the description.

HETEAC follows the Aerosol_cci approach and uses a component of strongly absorbing fine-mode particles with the same size distribution as for anthropogenic pollution and a constant refractive index of $m = 1.50 - 0.043i$. These microphysical properties lead to a lidar ratio of 117 sr at 355 nm and an extinction-related UV-VIS Ångström exponent of 1.25 (see Table 2). As can be seen from Fig. 2, the component does not represent typical smoke conditions, but sets an upper limit for the absorption and the resulting lidar ratio covered by the model. More realistic smoke properties can be simulated by mixing the strongly absorbing component with less absorbing fine and coarse particles. If a fraction of non-spherical coarse particles is added, a certain depolarization can be introduced as smoke typically shows linear depolarization ratios between 1 and 10 % in the troposphere (see Fig. 2). Mixing of components is further discussed in Sect. 6.4.

Table 4. Comparison of HETEAC, Aerosol_cci, and OPAC model values for effective radius (r_{eff}), lidar ratio at 355 nm (350 nm for OPAC, S_{UV}), and extinction-related Ångström exponents in the UV-VIS ($\hat{a}_{\text{ext,UV-VIS}}$) and VIS-IR range ($\hat{a}_{\text{ext,VIS-IR}}$) for anthropogenically polluted aerosol.

Relative humidity	$r_{\text{eff}}, \mu\text{m}$	S_{UV}, sr	$\hat{a}_{\text{ext,UV-VIS}}$	$\hat{a}_{\text{ext,VIS-IR}}$
HETEAC, fine mode, less absorbing				
	0.14	60.9	1.60	2.21
Aerosol_cci, fine mode, less absorbing				
	0.14	78.3	1.61	2.17
OPAC, polluted continental, three modes (<i>waso, inso, soot</i>)				
50 %	0.143	59.7	1.18	1.48
70 %	0.150	64.3	1.16	1.47
80 %	0.158	66.7	1.13	1.45
90 %	0.175	69.6	1.07	1.40
95 %	0.198	69.8	0.99	1.33
98 %	0.234	68.8	0.86	1.21
99 %	0.263	65.9	0.77	1.12
OPAC, urban, two modes (<i>waso, soot</i>)				
50 %	0.086	63.6	1.23	1.55
70 %	0.097	67.5	1.21	1.53
80 %	0.107	69.4	1.18	1.50
90 %	0.129	71.6	1.11	1.44
95 %	0.156	71.3	1.02	1.36
98 %	0.199	69.7	0.88	1.23
99 %	0.230	66.7	0.79	1.14

6.3.3 Spherical coarse-mode particles

Marine aerosol is primarily composed of water-soluble, coarse sea-salt particles generated by wind-driven physical processes at the ocean surface. Fine-mode particles consisting of non-sea-salt sulfates produced from organic precursor gases contribute to this aerosol type as well. Their number concentrations may be high, but their mass or volume fraction can usually be neglected against the sea-salt component. Except under very dry conditions (see Sect. 8.2), marine particles can be assumed to be spherical. The water content and thus size and refractive index of the particles depend on relative humidity. However, also in this case, HETEAC does not consider hygroscopic growth effects explicitly and defines only a typical coarse mode consisting of spherical particles. Again, the size-distribution parameters are taken from the Aerosol_cci model, but the refractive index is modified. While the Aerosol_cci model prescribes a constant value of $m = 1.40 - 0.0i$, HETEAC applies the spectral complex refractive index as suggested by OPAC for a moderate relative humidity of 70 % (see Fig. 4 and Table 3).

As for the weakly absorbing fine-mode particles, a sensitivity analysis regarding the influence of hygroscopic growth on optical parameters was performed with OPAC, and the optical data obtained from the different models were compared. Results are shown in Table 5. In OPAC, clean marine aerosol is defined as a three-modal composition of a water-soluble fine mode (*waso*), a sea-salt accumulation mode (*ssac*), and a sea-salt coarse mode (*sscm*). Refractive index and mode radius of all three modes change with relative humidity. To remove the influence of the fine-mode particles, calculation were also made for the two sea-salt modes only (*ssam*, *sscm*). From Table 5, it can be seen that the optical parameters vary only slightly in dependence on relative humidity and are all in good agreement with the observations (see Fig. 2). The lidar ratio at 355 nm calculated with OPAC is between 17 and 27 sr, i.e., in the expected range for large spherical, non-absorbing particles. Whereas the Aerosol_cci model gives a relatively small value of 13 sr due to the chosen refractive index, the adoption of the OPAC refractive index in HETEAC leads to a more realistic value of 18 sr.

Extinction-related Ångström exponents from OPAC are slightly negative and similar to the HETEAC and Aerosol_cci values, when only large sea-salt particles are considered. They become slightly positive when a water-soluble fine mode is added to the marine aerosol. Accordingly, also the lidar ratio is somewhat larger in the latter case. Also here, it should be mentioned that Zieger et al. (2013) showed that OPAC may overestimate the humidity-growth effects for moderate values of relative humidity. Nevertheless, it can be seen from Table 5 that the variability of the optical parameters of marine aerosol [under wet conditions](#) is anyhow small and on the order of the expected measurement errors. Thus, it is concluded that humidity-growth effects can be neglected in the classification of marine aerosol from spaceborne lidar observations and that the coarse sea-salt component proposed for HETEAC is a good representation of marine particles.

6.3.4 Non-spherical coarse-mode particles

Mineral dust is the aerosol with the highest abundance in the atmosphere. Most of the dust is emitted from deserts along the northern hemispheric dust belt, reaching from northern Africa with the Sahara as the largest global dust source over Middle East, Central Asia to China and Mongolia. Also deserts in North and South America, southern Africa and Australia contribute to the global dust load. Dust particles are of non-spherical shape, have a relatively large size, and their mineral composition varies depending on source region. Since the optical properties sensitively depend on actual size, shape, and complex refractive index, a proper selection of dust microphysical parameters for HETEAC is challenging, not only because of the natural variability of dust properties but also because of the limitations in the modeling of non-spherical particles (see Sect. 6.2.2). Therefore, a large number of simulations have been performed under consideration of a wide range of assumptions and parameters proposed in the literature.

Some representative results of these studies are shown in Fig. 5. The simulations have been performed with Dubovik's code for the two spheroid distributions shown in Fig. 3. Panels (a) and (b) of Fig. 5 show results at 355 nm for the size distribution proposed by Aerosol_cci, i.e., a constant effective radius of 1.94 μm , and a range of complex refractive indexes (orange symbols). As indicated in Fig. 4, mineral dust exhibits a considerably higher absorption in the UV than in the VIS and IR spectral range. The refractive index depends on mineral composition, and a variety of values can be found in the literature. A value of $1.56 - 0.005i$ at 355 nm has been proposed by Aerosol_cci, which leads to the $S-\delta$ positions encircled in red. OPAC

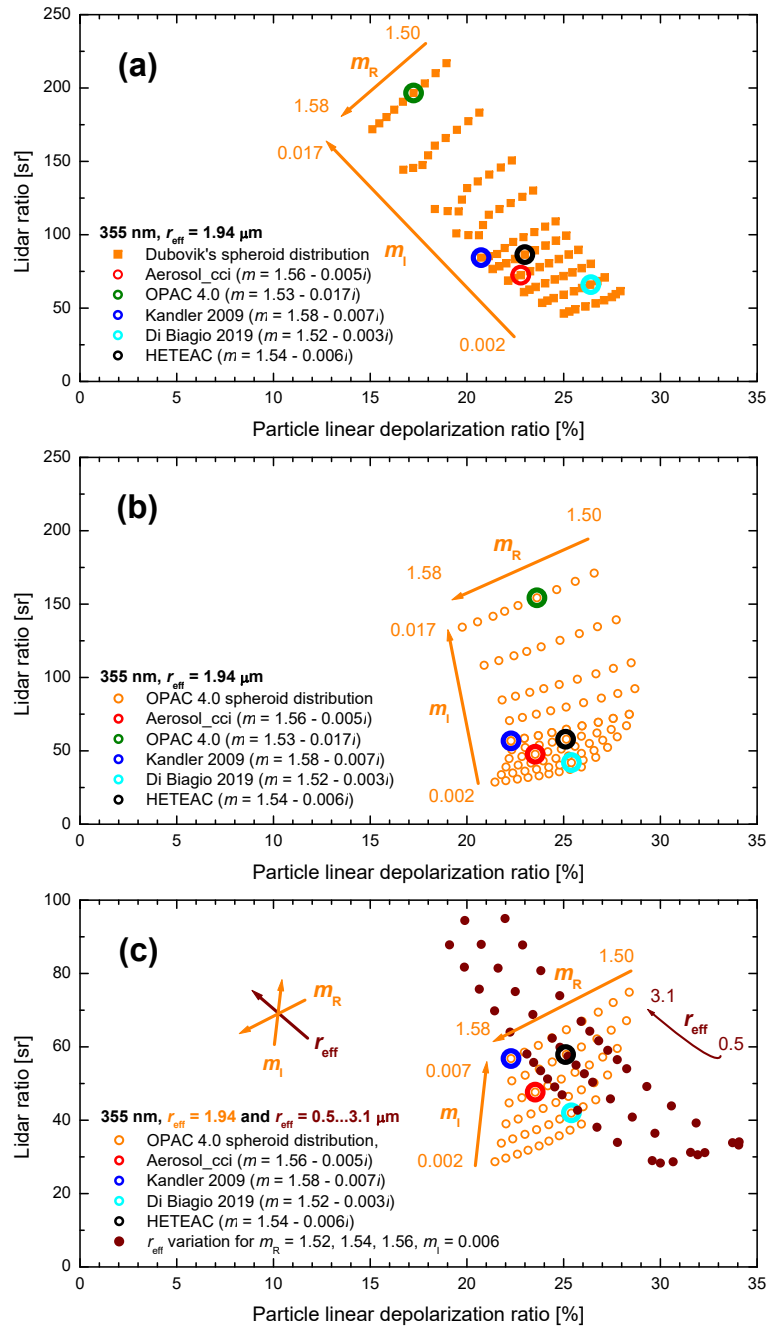


Figure 5. Simulated values of lidar ratio versus particle linear depolarization ratio at 355 nm for (a) the spheroid distribution after Dubovik et al. (2006) and (b and c) the spheroid distribution after Koepke et al. (2015). Orange symbols show results for a constant effective radius of $1.94 \mu\text{m}$ and varying complex refractive index as indicated in the figure. Dark brown symbols in panel (c) show results for varying effective radius.

Table 5. Comparison of HETEAC, Aerosol_cci, and OPAC model values for effective radius (r_{eff}), lidar ratio at 355 nm (350 nm for OPAC, S_{UV}), and extinction-related Ångström exponents in the UV-VIS ($\hat{a}_{\text{ext,UV-VIS}}$) and VIS-IR range ($\hat{a}_{\text{ext,VIS-IR}}$) for marine aerosol.

Relative humidity	$r_{\text{eff}}, \mu\text{m}$	S_{UV}, sr	$\hat{a}_{\text{ext,UV-VIS}}$	$\hat{a}_{\text{ext,VIS-IR}}$
HETEAC, coarse mode, spherical				
	1.94	18.1	-0.13	-0.20
Aerosol_cci, coarse mode, spherical				
	1.94	13.3	-0.12	-0.20
OPAC, clean marine, three modes (<i>waso, ssam, sscm</i>)				
50 %	0.803	22.7	0.14	0.13
70 %	0.923	22.7	0.13	0.10
80 %	1.031	26.1	0.12	0.08
90 %	1.267	21.0	0.12	0.06
95 %	1.590	27.4	0.12	0.06
98 %	2.207	23.1	0.10	0.07
99 %	2.836	23.2	0.08	0.06
OPAC, sea salt, two modes (<i>ssam, sscm</i>)				
50 %	1.227	18.7	-0.16	-0.09
70 %	1.379	18.6	-0.16	-0.12
80 %	1.516	21.7	-0.16	-0.13
90 %	1.808	17.0	-0.14	-0.15
95 %	2.197	22.8	-0.13	-0.16
98 %	2.902	19.1	-0.10	-0.12
99 %	3.575	19.8	-0.08	-0.10

(Koepke et al., 2015) proposes $1.53 - 0.017i$, i.e., a much higher imaginary part and thus a very strong absorption, resulting in unrealistically high lidar ratios of 150–200 sr for the two distributions (green circles). Kandler et al. (2009) calculated a value of $1.58 - 0.007i$ at 355 nm by analyzing the mass contributions of different minerals in dust samples from the Western Sahara
430 (blue circles). Di Biagio et al. (2019) derived complex refractive indexes from 19 samples collected in eight source regions worldwide. Their values range from 1.49 to 1.54 in real part (over the entire 370–950 μm wavelength range) and from 0.0011 to 0.0088 in imaginary part at 370 nm, with a global mean value of $1.52 - 0.0033i$ in the UV (cyan circles). By comparing panels (a) and (b) of Fig. 5 with the experimental basis in Fig. 2, it can be seen that with the spheroid distribution proposed in OPAC 4.0, which follows from the measurements provided by Kandler et al. (2009), a good agreement between measured and
435 simulated values for a realistic range of refractive indexes is found, while the spheroid distribution after Dubovik et al. (2006) leads to much higher lidar ratios than typically observed.

In panel (c) of Fig. 5, a subset of values from panel (b) ($r_{\text{eff}} = 1.94 \mu\text{m}$, $m_{\text{R}} = 1.50\text{--}1.58$, $m_{\text{I}} = 0.002\text{--}0.007$) is shown and compared with results for varying effective radius at three selected values of refractive index. The dark brown symbols span a relatively wide range of effective radii from 0.5 to 3.1 μm . AERONET data indicate that the effective radius of the dust coarse mode is typically between 1 and 2.7 μm (see, e.g., Holzer-Popp et al., 2013, Fig. 1 and 2). In this size range, for constant refractive index, an increase of the effective radius leads to an increase of the lidar ratio and a decrease of the linear depolarization ratio. In general, we see that for the assumed spheroid distribution, a variation of real and imaginary part of refractive index and of effective radius shifts the $S\text{--}\delta$ points in the diagram in three different directions and, thus, the natural variability around typical values of $S = 50$ sr and $\delta = 25\%$ as found from observations can be well covered with the simulations.

Even if the model seems to work fine at the wavelength of 355 nm, we have to be careful regarding the spectral behavior of the simulated values. Figure 6 shows Ångström exponents calculated for the wavelength pair 355 and 532 nm. As in Fig. 5b, the spheroid distribution after Koepke et al. (2015) and an effective radius of 1.94 μm was used. The refractive index at 355 nm was fixed to $m = 1.54 - 0.006i$. The extinction-related and backscatter-related Ångström exponents were then computed for a varying refractive index at 532 nm. In all cases, negative values of the Ångström exponent are found. While the extinction-related Ångström exponent is insensitive to changes of the refractive index and almost constant at -0.1 , the backscatter-related Ångström exponent is strongly dependent on the refractive index and shows large negative values. For instance, for the refractive index of $1.53 - 0.003i$ chosen for HETEAC (see Fig. 4 and Table 3), the backscatter-related Ångström exponent becomes -1.6 . As a consequence, the modeled lidar ratio at 532 nm is much smaller than at 355 nm. For the parameters selected for HETEAC, we obtain 58 sr at 355 nm and 31 sr at 532 nm. In principle, negative dust Ångström exponents are not unusual in nature, but values below -1 seem unrealistic. For instance, Veselovskii et al. (2020) reported backscatter-related Ångström exponents down to -0.75 for measurements in West Africa and also discussed the dependence of the values on the wavelength-dependent imaginary part of the refractive index. The observational mean values from our experimental basis are typically close to 0, with slightly positive extinction-related Ångström exponents of 0.1 and 0.2 and slightly negative backscatter-related Ångström exponents of 0.0 and -0.2 for Saharan and Central Asian dust, respectively (Floutsi et al., 2022). Accordingly, the measured lidar ratios at the two wavelengths are similar, with values of about 53 sr for Saharan dust at both wavelengths and 43 and 38 sr for Central Asian dust at 355 and 532 nm, respectively (Floutsi et al., 2022). The model can reproduce this spectral behavior only, when unrealistically low real parts and high imaginary parts of refractive index at 532 nm are assumed (see values in the upper left corner of Fig. 6). We argue that the spheroidal particle shape model is not able to fully mimic the scattering properties of irregularly shaped dust particles at 180° . Specific features for exact backscattering, similar as known for spheres, could play a role. These limitations may be overcome in future with more realistic scattering models for irregularly shaped particles (see Sect. 8.4).

Keeping the limitations of the scattering model for non-spherical particles in mind, we can conclude that a satisfying representation of dust is obtained in HETEAC with the parameter settings for non-spherical coarse particles as provided in Table 2 and under consideration of the experimentally derived spheroid distribution as proposed for OPAC 4.0 (Koepke et al., 2015). Humidity-growth effects do not play a role for dust particles and can be neglected (Denjean et al., 2015). The selected refrac-

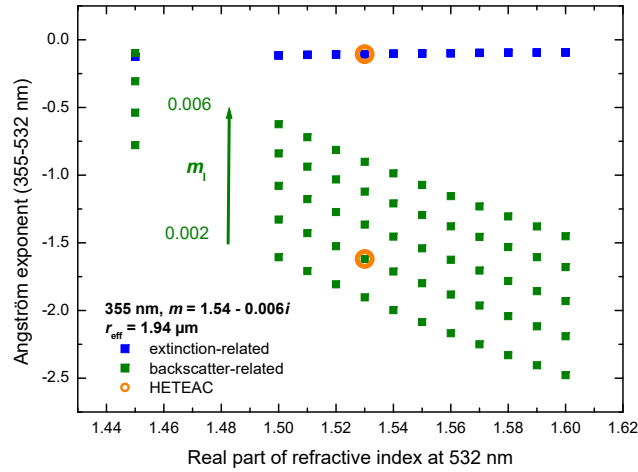


Figure 6. Simulated values of the extinction-related (blue) and backscatter-related Ångström exponents (green) for the 355-to-532 nm wavelength pair. The spheroid distribution after Koepke et al. (2015), the effective radius of $1.94 \mu\text{m}$, and the refractive index of $m = 1.54 - 0.006i$ at 355 nm are kept constant, while the refractive index at 532 nm is varied as indicated.

Refractive index of $m = 1.54 - 0.006i$ is tuned to best represent observations of Saharan dust as the most abundant type (see Fig. 2). For specific studies, such as radiative closure assessments, it might be necessary to adapt the refractive index according to the source region.

475 6.4 Definition of component mixtures

As shown above, major aerosol types like anthropogenic pollution, fresh smoke, sea salt, and dust can be described with four basic aerosol components consisting of two fine and two coarse particle modes, each with predefined particle shape (distribution) and complex refractive index. The four components define the optical parameter space (corner points) that is covered with the model. The microphysical properties of the components have been selected such that an optimum overlap
480 between model and observation space in terms of optical data is obtained. By mixing the four basic components, we can fill the model space in between the corner points and thus compose new or mixed aerosol types in accordance with the observations.

For this purpose, we assume an external mixture of the particles and apply mixing rules to obtain the intensive optical parameters of multimodal aerosol compositions. Starting from the microphysical parameters of each component, the individual scattering properties per unit particle volume (e.g., $1 \mu\text{m}^3 \text{cm}^{-3}$) are calculated with the respective scattering model first. Then,
485 the optical parameters of interest are derived from the extinction, scattering, and backscatter coefficients per unit volume ($\bar{\alpha}_i$, $\bar{\beta}_i$, and $\bar{\sigma}_i$, respectively), the depolarization ratio δ_i , and the relative volume contribution v_i of each mode i . In this way, we obtain, e.g., the lidar ratio

$$S = \frac{\sum_i v_i \bar{\alpha}_i}{\sum_i v_i \bar{\beta}_i} \quad (6)$$

and the particle linear depolarization ratio

$$490 \quad \delta = \frac{\sum_i v_i \bar{\beta}_i \frac{\delta_i}{1+\delta_i}}{\sum_i v_i \bar{\beta}_i \frac{1}{1+\delta_i}} \quad (7)$$

of the mixture.

Figure 7 shows the S - δ diagram at 355 nm for bimodal and trimodal mixtures. The stars indicate the pure components. The numbers stand for the volume mixing ratio in percent. It can be seen that the depolarization ratio of dust (orange stars) sensitively reacts to the addition of non-depolarizing particles. The dependence is non-linear in terms of particle volume contribution, i.e., the mixing of dust with fine-mode particles or sea salt can be well resolved as long as the dust contribution dominates. Vice versa, a relatively large amount of dust is needed to cause a considerable depolarization ratio. Similarly, very large and very small lidar ratios are only obtained when the absorbing or the sea-salt components dominate, respectively. Many of the mixtures produce lidar ratios of 50–70 sr and particle linear depolarization ratios below 5%. Such values are indeed most often observed in nature and are typical for polluted continental sites (see Fig. 2).

500 6.5 Modeling of radiative properties

If the aerosol typing is used for radiation studies, the radiative properties of the aerosol components and their mixtures are needed. Radiative transfer models typically require input information on particle size (e.g., in terms of effective radius or asymmetry parameter) and on scattering and absorption properties (i.e., complex refractive index or single-scattering albedo) over the relevant spectral range. Furthermore, in the case of EarthCARE, the extinction profile measured with ATLID at 355 nm must be converted to the input wavelength used in the model (e.g., 550 nm) by applying appropriate (vertically resolved) Ångström exponents.

To support radiative transfer calculations, HETEAC provides an LUT of radiative parameters for the four pure aerosol components and their mixtures. Again, external mixing rules are applied to calculate the Ångström exponent

$$510 \quad \dot{a} = \frac{\ln \left(\frac{\sum_i v_i \bar{\alpha}_{i,\lambda_1}}{\sum_i v_i \bar{\alpha}_{i,\lambda_2}} \right)}{\ln(\lambda_2/\lambda_1)}, \quad (8)$$

the single-scattering albedo

$$\omega_0 = \frac{\sum_i v_i \bar{\sigma}_i}{\sum_i v_i \bar{\alpha}_i}, \quad (9)$$

and the asymmetry parameter

$$g = \frac{\sum_i v_i \bar{\sigma}_i g_i}{\sum_i v_i \bar{\sigma}_i}. \quad (10)$$

The calculations are performed for lidar wavelengths of 355, 532, and 1064 nm and imager wavelengths of 670, 865, 1650, and 2210 nm, as well as for 550 nm. The parameters are given for 314 mixtures with equally distributed volume fractions of

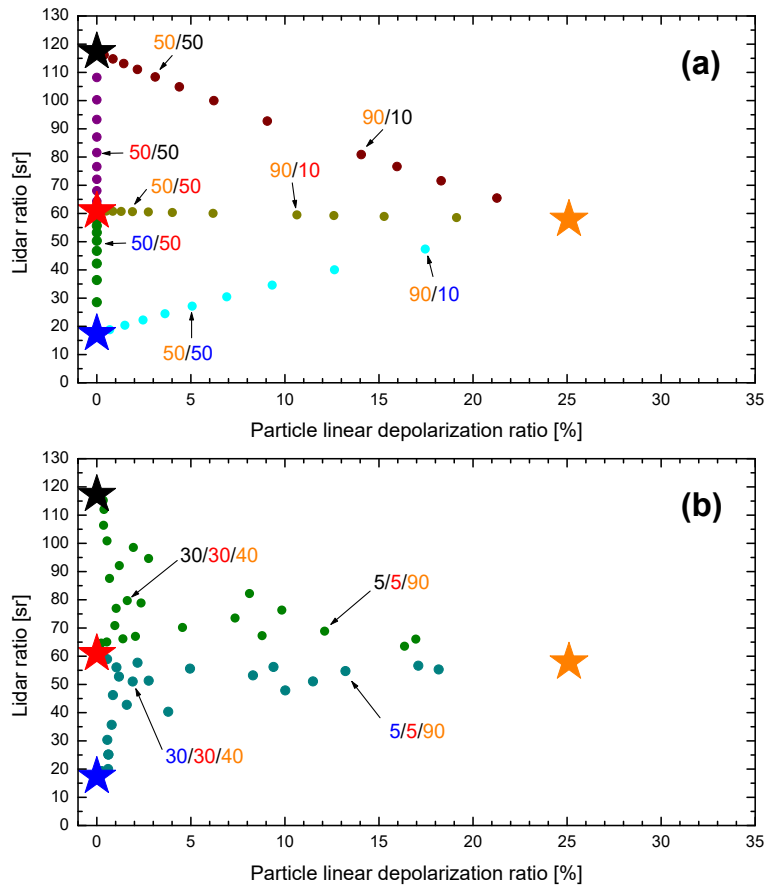


Figure 7. Simulated values of lidar ratio versus particle linear depolarization ratio at 355 nm for (a) mixtures of two components and (b) mixtures of three components. The pure components are indicated by stars (red = fine mode, weakly absorbing; black = fine mode, strongly absorbing; blue = coarse mode, spherical; orange = coarse mode, non-spherical), and their properties are given in Table 2. The numbers in the plots show the mixing state in terms of particle volume in percent (colors as for the stars).

the components of 0 %, 5 %, 10 %, 20 %, 30 %, . . . , 90 %, 95 %, 100 %. Results for the 355-to-670 nm Ångström exponent as well as for the single-scattering albedo and asymmetry parameter at 550 nm are shown in Fig. 8. The values are color-coded and projected into the S - δ diagram to illustrate how the typing via the lidar measurements can be used to select proper data for radiative transfer calculations. It can be seen that the assignment works best when the aerosol mixture is dominated by coarse particles (either high depolarization ratio or low lidar ratio) or by strongly absorbing particles (high lidar ratio), while ambiguities occur for low depolarization ratios and medium lidar ratios, in particular regarding the single-scattering albedo.

Further discussion on implications of the model assumptions on mixing state and other limitations as well as possible improvements and needs for further developments is provided in Sect. 8. The LUT with the optical and radiative properties of the 314 mixtures at the eight wavelengths of interest can be found in Wandinger et al. (2023a).

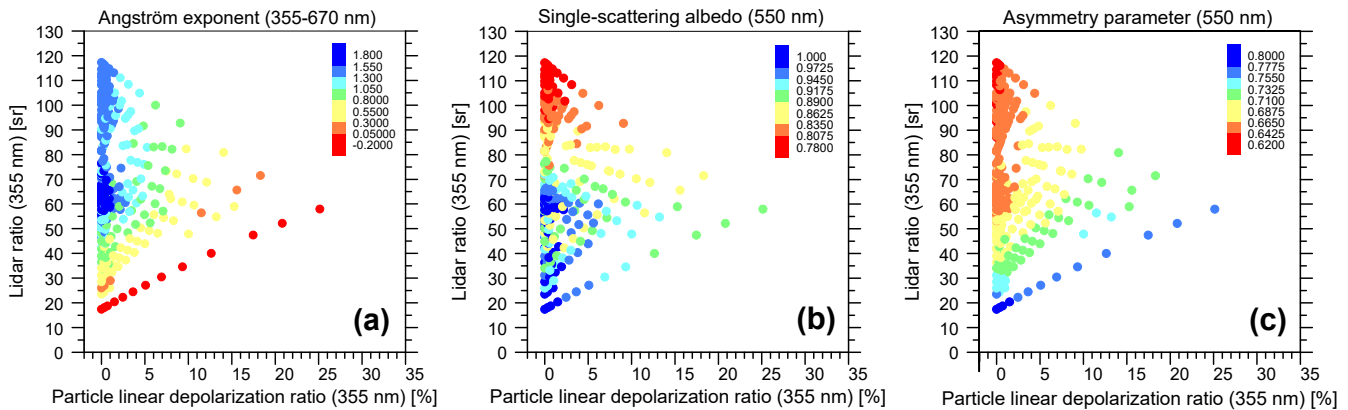


Figure 8. Simulated values of (a) Ångström exponent for the 355-to-670 nm spectral range, (b) single-scattering albedo at 550 nm, and (c) asymmetry parameter at 550 nm. The values are color-coded and projected into the S - δ plane at 355 nm (see legends).

525 7 Applications of HETEAC

HETEAC is or will be applied in the development of EarthCARE retrieval algorithms, the generation of test scenes for algorithm performance evaluation, as well as for data evaluation and radiation closure studies. In the following, a brief overview on applications that are important for the preparation of the mission is given. In Sect. 7.1, the use of HETEAC in the generation of ECSIM aerosol scenes is explained, while Sect. 7.2 shows its application in the retrieval of various EarthCARE stand-alone and synergistic aerosol products.

7.1 Simulation of aerosol test scenes

Artificial atmospheric scenes have been extensively used to test the performance of the EarthCARE algorithms during their development. For this purpose, three dedicated scenes (entitled *Halifax*, *Baja*, and *Hawaii*) were generated based on output of the Global Environmental Multiscale (GEM) model (Qu et al., 2022b; Donovan et al., 2023b). Each scene represents a typical EarthCARE frame of about 5000 km length, corresponding to one eighth of an entire orbit, which is the standard for EarthCARE data processing (Eisinger et al., 2023). Since GEM does not provide aerosol forecasts, supplementary information was taken from the Copernicus Atmosphere Monitoring Service (CAMS) model. The CAMS aerosol component fields, containing sea salt, dust, organic and black carbon, and sulfate aerosol, were mapped in an ad hoc fashion to the HETEAC components of coarse spherical, coarse non-spherical, strongly absorbing fine-mode, and weakly absorbing fine-mode particles, respectively (see Qu et al., 2022b, for details). This procedure was successful in creating aerosol fields in ECSIM with a realistic range of extinction, lidar ratio, and AOT at the ATLID and MSI wavelengths, which were then applied to test the stand-alone and synergistic aerosol retrievals (e.g., Donovan et al., 2023a; Wandinger et al., 2023b; Docter et al., 2023; Haarig et al., 2023; Mason et al., 2022). An example is provided in the next section.

7.2 Aerosol classification in EarthCARE retrievals

545 7.2.1 ATLID aerosol retrievals: the A-TC product

The ATLID Target Classification (A-TC) algorithm, which produces the corresponding A-TC product, is part of the ATLID L2a Profiles (A-PRO) processor and is explained in detail by Donovan et al. (2023a). The A-TC approach works with aerosol types (i.e., target classes for aerosol) that are described as mixtures of the four basic HETEAC aerosol components. The joint S - δ distribution for each aerosol type is modeled using a Gaussian probability distribution defined by a mean lidar ratio, particle
550 linear depolarization ratio, their associated Gaussian widths and correlation. Figure 9 shows the S - δ probability distribution functions (PDFs) schematically. Based on the HETEAC information on the S - δ distribution for pure and mixed components (Fig. 7) and in agreement with the experimental basis (Fig. 2), six aerosol types corresponding to marine aerosol, continental pollution, smoke, dust, dusty smoke, and dusty aerosol mixtures are defined such that the PDFs span the same phase space as the HETEAC model and the lidar observations. At the same time, they are well separated from the expected distribution for
555 ice crystals, i.e., the methodology also supports aerosol-cloud discrimination. The volume and extinction mixing ratios for the six aerosol types used in the algorithm developments are presented in Table 6. These values will be further refined based on algorithm tests with experimental data in the future.

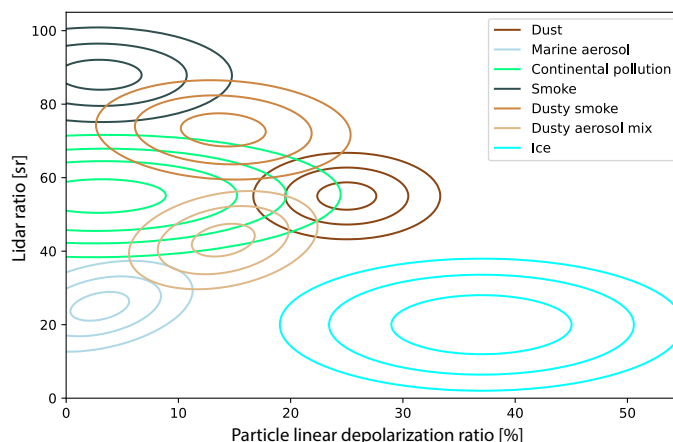


Figure 9. Schematic representation of the S - δ probability distribution functions used to determine the aerosol-related elements of the A-TC product.

An example aerosol classification result is shown for the *Halifax* scene in Fig. 10. According to the CAMS output, sulfate and sea-salt aerosols were present in the atmosphere. Respective extinction fields of weakly absorbing fine-mode and spherical
560 coarse-mode particles were generated with ECSIM, which represent the model truth for the aerosol typing (lowermost two left panels). The entire extinction field of the *Halifax* scene including clouds, aerosols, and precipitation is shown in the upper left panel. By comparing the A-TC results (bottom-right panel) with the model truth, it can be seen that, overall, the A-TC results capture the presence of two distinct main aerosol types in the southern segment (right part) of the frame. In the northern

Table 6. Volume mixing ratios (VMR) and extinction mixing ratios (EMR) corresponding to the six tropospheric A-TC aerosol types shown in Fig. 9.

	Fine mode		Fine mode		Coarse mode		Coarse mode	
	weakly absorbing		strongly absorbing		spherical		non-spherical	
	VMR	EMR	VMR	EMR	VMR	EMR	VMR	EMR
Dust	0.015	0.13	0.00	0.00	0.02	0.02	0.965	0.85
Marine aerosol	0.00	0.00	0.00	0.00	0.99	0.99	0.01	0.01
Continental pollution	0.35	0.85	0.00	0.00	0.54	0.12	0.10	0.02
Smoke	0.19	0.22	0.59	0.76	0.00	0.00	0.21	0.02
Dusty smoke	0.00	0.00	0.12	0.61	0.00	0.00	0.88	0.39
Dusty aerosol mix	0.05	0.36	0.00	0.00	0.40	0.26	0.55	0.38

segment, the aerosols are largely obscured by the extended areas of high cloud coverage. Misclassifications and unknown-type
565 determinations are related to noise and errors in the input A-PRO lidar ratios and particle linear depolarization ratios used by
the classification procedure (uppermost two right panels). These input data are stored in the ATLID Extinction, Backscatter
and Depolarization (A-EBD) product. Their generation, including the applied horizontal averaging strategy, is described in
Donovan et al. (2023a). The algorithm works on a layer basis and provides the data with three different horizontal resolutions
(between 1 and 150 km) adapted to the specific scene. These three resolutions are always the same for all products to make
570 them usable in combination downstream in the processing chain. From the simulations, it is expected that retrievals of layer-
average optical properties, and thus aerosol typing, can be done for minimum extinction values on the order of $5.0 \times 10^{-6} \text{ m}^{-1}$
on the 50–100 km horizontal scale.

The aerosol classification from A-TC is reproduced in the ATLID–CPR synergistic target classification product (AC-TC,
Irbah et al., 2022) later in the processing chain. There, the only modifications occur in rare instances where CPR detections
575 may help distinguish ice from aerosols. AC-TC is the basis for further synergistic retrievals explained in Sect. 7.2.5.

7.2.2 ATLID aerosol retrievals: the A-ALD product

The ATLID Aerosol Layer Descriptor (A-ALD) algorithm, which generates the A-ALD product, is part of the ATLID L2a
Layer Products (A-LAY) processor described in Wandinger et al. (2023b). The algorithm detects aerosol layer boundaries
and calculates the layer-mean optical properties such as backscatter coefficient, extinction coefficient, lidar ratio, and particle
580 linear depolarization ratio. The latter two might be used as input for an aerosol classification per layer based on HETEAC in a
similar way as done in the A-TC algorithm (Donovan et al., 2023a). However, in the A-LAY processor a different approach is
implemented to prepare the synergy with MSI, for which columnar values are needed (see Sect. 7.2.3). Thus, column-integrated
aerosol classification probabilities are derived from the A-TC product. For this purpose, the relative contribution of each of the
six A-TC aerosol types to the total AOT at 355 nm is calculated by weighting the probability of occurrence for each height

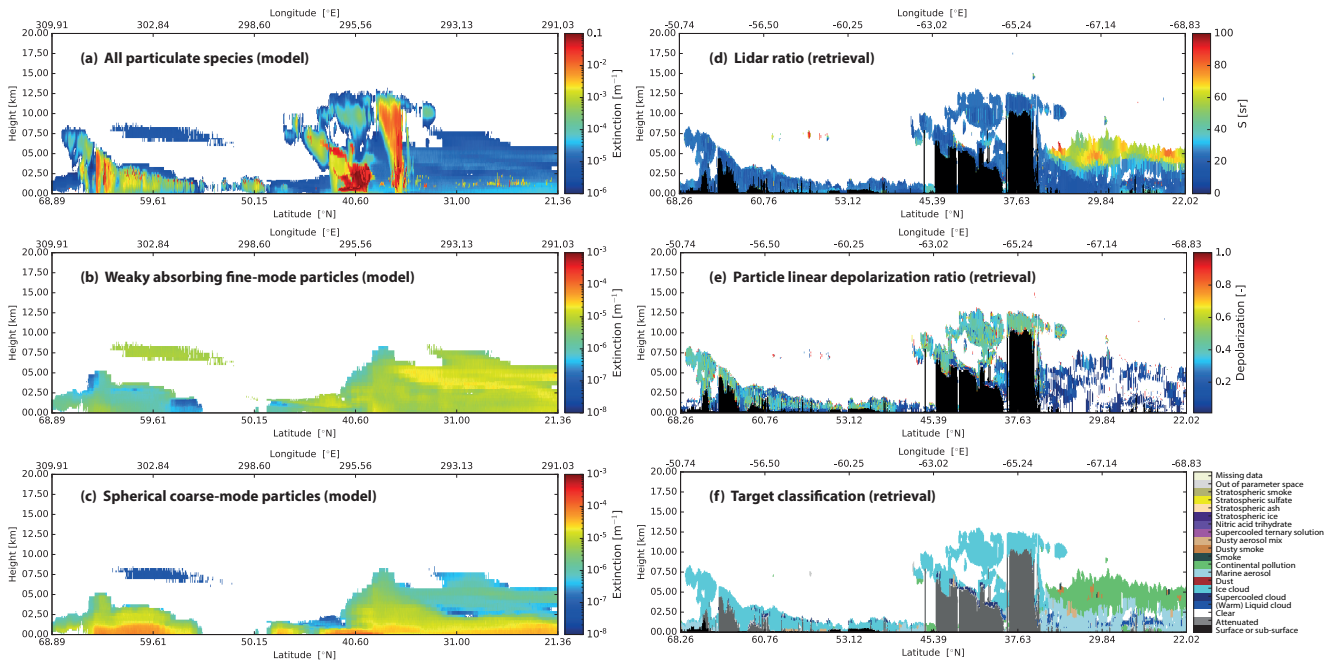


Figure 10. Aerosol classification for the *Halifax* scene. Panel (a) shows the modeled nadir total extinction field including all aerosol, cloud, and precipitation types. Panels (b) and (c) display the modeled extinction fields for weakly absorbing fine-mode particles (the primary component of the A-TC type “continental pollution”) and spherical coarse-mode particles (the primary component of the A-TC type “marine aerosol”), respectively. Panels (d) and (e) show the fields of lidar ratio and particle linear depolarization ratio, respectively, retrieved with A-PRO and stored in the A-EBD product. These values are used together with the predefined S - δ PDFs (shown in Fig. 9) to determine the aerosol-related elements of the A-TC product depicted in panel (f). Note that the longitude is defined in the interval $[0^\circ \text{ E}, 360^\circ \text{ E}]$ in the model (left panels) and $[-180^\circ \text{ E}, 180^\circ \text{ E}]$ in the [EarthCARE productsretrieval](#) (right panels).

585 bin with the respective extinction coefficient at 355 nm and integrating this information over the entire profile (see Fig. 10 in [Wandinger et al., 2023b, for an example](#)). The column-integrated aerosol classification probabilities can then be compared with the aerosol-type results of the MSI retrieval (see Sect. 7.2.3 and 7.2.4).

7.2.3 MSI aerosol retrievals: the M-AOT product

590 The MSI L2a Aerosol Optical Thickness (M-AOT) retrieval, which produces the M-AOT product (Docter et al., 2023), uses an approach based on LUTs for its forward model. The LUTs rely on radiative transfer simulations with the Matrix Operator model MOMO (Hollstein and Fischer, 2012; Fell and Fischer, 2001), for which the optical properties of the four HETEAC components are used. To allow for the presence of more than one pure HETEAC component within a column, the four components have been additionally mixed via their contribution to aerosol optical thickness. For this purpose, 25 HETEAC-based component mixtures

have been defined. The choice of the most appropriate mixture to be used in the retrieval is then based on climatological
595 knowledge over land and on the best-fitting mixing above ocean (Docter et al., 2023).

While ATLID-based retrievals provide direct information on the type or mixtures, the imager-based retrieval is not able to
do so due to the limited information available from MSI. At best, the M-AOT retrieval can distinguish between coarse and
fine modes and respective mixtures over ocean, based on the spectral behavior of AOT determined from the four bands of the
so-called VNS (visible, near-infrared, and short-wave infrared) camera of MSI and the low surface contribution to the signal in
600 off-glint regions. On the other hand, the classification of the sub-types sea salt (spherical) or dust (non-spherical) and weakly
absorbing or strongly absorbing fine mode is much more difficult, because of the similarity in the optical properties that are
accessible with MSI measurements. Hence, the retrieved AOT is always accompanied by the used HETEAC aerosol component
mixture in the M-AOT product. In this way, users may be able to apply ad-hoc corrections to M-AOT estimates at 670 and
865 nm.

605 **7.2.4 Synergistic aerosol retrievals: the AM-ACD product**

The ATLID–MSI Aerosol Column Descriptor (AM-ACD) is produced by the ATLID–MSI L2b Column Products (AM-COL)
processor, which is described in detail by Haarig et al. (2023). The algorithm compares the aerosol typing of ATLID (A-TC,
Sect. 7.2.1; A-ALD, Sect. 7.2.2) and MSI (M-AOT, Sect. 7.2.3) along the satellite track and thus provides a quality check
and additional information for users with respect to the limited MSI information. To facilitate the comparison, the dominant
610 aerosol type of each typing scheme is determined. The dominant aerosol type is defined by the highest column-integrated
aerosol classification probability (ATLID) and the component with highest contribution to the aerosol mixing ratio (MSI),
respectively. The four pure types of A-TC are dominated by the four aerosol components defined in HETEAC and used in M-
AOT, respectively. Thus, their contributions can be directly compared. The challenge arises from the two mixed types in A-TC,
“dusty mix” and “dusty smoke”, which have to be converted back into the basic HETEAC components. Such a conversion can
615 be done with the help of the mixing rules described in Sect. 6.4 and the PDFs, which define mixed types. Details and further
discussion are provided in Haarig et al. (2023).

7.2.5 Synergistic aerosol retrievals: the ACM-CAP product

The ATLID–CPR–MSI L2b Cloud, Aerosol and Precipitation (ACM-CAP) processor, which generates the respective ACM-
CAP product, carries out a retrieval of the aerosol classes identified in the synergistic target classification (AC-TC, see last
620 paragraph of Sect. 7.2.1), constrained by the synergy of ATLID and MSI solar and thermal IR channels. The ACM-CAP
algorithm takes a different approach from those taken in A-PRO, in that the size distributions and physical properties of the
aerosol types, including their lidar ratio, are predetermined entirely by the A-TC classification (i.e., by the volumetric mixtures
of the four pure HETEAC components given in Table 6). Only the profile of particle number concentration is retrieved for
each aerosol class, which scales the retrieved extinction and aerosol optical depth. To constrain the retrieval of horizontally
625 homogeneous aerosol fields from inherently noisy lidar measurements at the scale of the joint standard grid, a Kalman smoother

is applied such that the retrieved quantities in each profile are constrained by the values in adjacent profiles. A more detailed description and evaluation of the ACM-CAP aerosol retrieval is given in Mason et al. (2022).

7.2.6 Radiative closure assessments: the ACM-RT product

Inclusion of aerosols into EarthCARE’s radiative closure assessments (Barker et al., 2023) requires they be specified in the forward radiative transfer calculations (Cole et al., 2022). The specification is done following the HETEAC model. For the basic aerosol components, specific extinction (for solar), specific absorption (for thermal), single-scattering albedo, and asymmetry parameter are computed for 166 wavelengths between 0.2 and 400 μm . The single-scattering properties are then combined into the aerosol types using external mixing and volume mixing ratios according to Table 6. The single-scattering albedo and asymmetry parameter for the mixtures are computed following Eq. (9) and (10), respectively. Rather than use specific extinction and absorption for each wavelength and mixture, values for each mixture are normalized by the mixture extinction at 355 nm. This normalization allows these to be scaled by the ATLID extinction profile (Donovan et al., 2023a) when computing the optical properties for the radiative transfer calculations.

The radiative transfer models used to generate the ATLID–CPR–MSI Radiative Transfer (ACM-RT) product work with optical properties averaged over wavelength intervals (Cole et al., 2022). Averaging of the aerosol single-scattering optics over the intervals was done using wavelength-specific weighting. Weightings for solar wavelength intervals were downwelling irradiances averaged at the tropopause and surface from line-by-line data (Iacono et al., 2008) for a tropical atmosphere at a solar zenith angle of zero degrees. For thermal wavelength intervals, weightings were the Planck function at 275 K.

8 Discussion

In this section, we discuss some further implications following from simplifying model assumptions and current limitations of HETEAC. As explained in Sect. 2, we aimed at a complete enough but not too complicated aerosol classification model, which can serve multiple purposes in the course of EarthCARE development works. The applications shown in Sect. 7 demonstrated that this goal has been successfully reached. However, when dealing with real-world data later on, we will be confronted with questions and shortcomings, which will require specific validation efforts on the one hand and improvements of HETEAC on the other hand. We tackle some aspects that are already foreseen in the following.

8.1 Ambiguities of the S – δ phase space

Major ambiguities of aerosol typing by using the S – δ phase space at the single ATLID wavelength of 355 nm result from the similarity of optical fingerprints with low particle linear depolarization ratio ($\delta < 5\%$) and medium lidar ratio (S between 40 and 70 sr). Such values can be caused by different particle blends and will in particular impede a clear separation of aged tropospheric smoke and continental pollution. As a consequence, a proper assignment of the single-scattering albedo for radiative transfer calculations and closure assessments is difficult (see Fig. 8b). Additional criteria such as geographical location and altitude of aerosol layers, supported by source analysis, are required for an advancement of the typing in these cases and

may be considered in future upgrades of the EarthCARE retrieval schemes. In general, an in-depth validation with ground-based and airborne observations is needed after the launch of the mission to evaluate the aerosol classification results and their application in radiative closure studies. Ground-based and airborne lidar instruments that measure extinction, backscattering, and depolarization at multiple wavelengths (typically 355, 532, and 1064 nm) and ideally also have a fluorescence detection capability for the identification of organic materials (contained in smoke and biogenic particles) are best suited to provide a comprehensive aerosol classification for validation purposes, because they are able to resolve the ambiguities that result from the limited information content of the ATLID measurements at a single wavelength.

8.2 Specific aerosol types

The four basic aerosol components and their mixtures considered in HETEAC do not cover very specific categories of particles that may occur in the atmosphere under certain conditions. Some examples are included in the experimental data base (Floutsi et al., 2022) and show where further ambiguities and misclassifications can happen.

For instance, sea-salt particles change their shape from spherical to cubic under dry conditions. Thin layers of depolarizing particles are sometimes observed at the top of the marine boundary layer, when it is in contact with the dry free troposphere (Haarig et al., 2017b). Thomas et al. (2022) reported increasing depolarization ratios towards the sea surface in CALIOP observations over the Southern Ocean, when the relative humidity in the marine boundary layer was below 60 % in wintertime. Since the depolarization ratio of cubic salt particles is much smaller (around 8 % at 355 nm, Haarig et al., 2017b) than that of dust, the model will describe the aerosol would be classified as a mixture of spherical and non-spherical coarse-mode particles. Because of this ambiguity in the optical parameters, identification of dry sea salt would require an additional screening of atmospheric scenes for such features these specific layers under consideration of auxiliary humidity information. Yet, it is unclear whether the resolution of ATLID is good enough to detect them at all. Therefore, we aim at further investigations of this effect when the mission is in space.

Similarly, freshly emitted volcanic ash particles in the troposphere may be interpreted as dust because of their high depolarization ratio. Even if the few available observations indicate that ash could be separated from dust by a higher depolarization ratio (see Floutsi et al., 2022, Fig. 2), the number of observations is too sparse and the microphysical representation in the model too uncertain to define an extra ash component in HETEAC at the moment.

Other aerosols that may need extra treatment in applications are Arctic haze, which consists of strongly aged particles with a characteristic size distribution, East and Southeast Asian haze, caused by extreme industrial and/or biomass-burning emissions and photochemical processing, or biogenic particles like pollen, which can show dust-like fingerprints due to their large size and non-spherical shape. Whether it is worthwhile to include such specific types in the EarthCARE aerosol classification scheme can only be decided by evaluating the quality and information content of the EarthCARE data in the course of the mission.

8.3 Mixing state and humidity growth effects

Mixing rules in HETEAC are based on the assumption of external aerosol mixtures, i.e., the different particles maintain their individual physical and chemical properties while being located in the same scattering volume. This assumption is well justified

690 in many cases, in particular for the mixing of coarse and fine particles such as dust and smoke or sea salt and pollution, and is reflected in typical bimodal or multi-modal size distributions obtained from in situ and remote-sensing measurements. Nevertheless, effects of internal mixing should be kept in mind. As already discussed in Sect. 6.3.2, particles originating from combustion processes undergo chemical and physical processing during and after emission. They change their properties over their lifetime and may be composed of soluble and insoluble materials. Such an internal structure is often accounted
695 for by applying a core-shell model for the calculation of optical properties, i.e., the particle is modeled as consisting of a spherical, insoluble, absorbing core surrounded by a liquid solution. A major result of such investigations is the enhancement of absorption, and thus the decrease of the single-scattering albedo, when the same amount of black carbon is assumed to be contained as a core within a water-soluble shell instead of making up a separate fraction of particles (e.g., Jacobson, 2000, 2001; Lesins et al., 2002; Cappa et al., 2012; Li et al., 2022). However, Cappa et al. (2012) also showed that this effect
700 may be overestimated by the idealized spherical geometry and is probably less pronounced in reality.

Another aspect that has to be considered regarding the mixing state is its influence on the hygroscopic growth of particles. The studies with OPAC presented in Sect. 6.3.1 and 6.3.3 are based on external mixing of soluble and insoluble components and showed that changes in the lidar ratio due to water uptake may be on the order of 10–20 % and thus play a minor role for aerosol typing based on HETEAC. Veselovskii et al. (2020) reported similar changes of the 355 nm lidar ratio for African
705 biomass-burning aerosol. They observed increasing values from 62–80 sr for increasing relative humidity from 25–85 %, which could be well explained with the modeled behavior of hygroscopic, absorbing, homogeneous spheres. Düsing et al. (2021) determined higher lidar-ratio enhancement factors by applying a core-shell scattering model to measured in situ data. For continental European aerosol, they found an increase of the 355 nm lidar ratio by a factor of 1.3 and 1.6, when the relative humidity increased from 50 to 80 % and from 50 to 90 %, respectively.

710 The investigations on the effects of internal mixing described above are limited to case studies and the methods have large uncertainties. Thus, it is difficult to draw general conclusions for HETEAC. Overall, the assumption of an external aerosol mixture may not always be appropriate. However, the discussed effects of enhanced absorption and hygroscopic growth are mainly related to internal mixing of fine-mode particles and thus contribute together with all other chemical and physical variations to their overall bulk appearance in the atmosphere, for which the model is actually designed. EarthCARE data with
715 their limited information content will only allow the identification of more and less absorbing fine-mode aerosols and the discrimination of coarse-mode aerosols. For this purpose, the approach of external mixing is appropriate, sufficiently robust, and well supported by the experimental data from ground-based observations. [However, it is suggested that the validation experiments also consider the aspects of aerosol mixing state and humidity growth and provide recommendations for necessary improvements of the HETEAC model and the associated algorithms.](#)

720 **8.4 Modelling of non-spherical particles**

Further improvements of HETEAC are desirable for the modeling of non-spherical particles. In general, a more realistic representation of particle shapes in scattering models is an urgent issue to answer open questions on relations between dust microphysical and optical properties. Experimental studies on relationships between lidar ratio and dust composition (i.e.,

refractive index, see Schuster et al., 2012; Veselovskii et al., 2020) are based on retrievals that make use of the spheroid
725 scattering model and shape distribution provided by Dubovik et al. (2006). As shown in Sect. 6.3.4, the model does not properly
reflect the backscatter spectral behavior of natural dust. Discrepancies between dust optical properties directly measured with
lidar at three wavelengths and those derived from AERONET observations by applying the spheroid model were also reported
by Haarig et al. (2022). Thus, care must be taken in interpreting any results that rely on the application of a scattering model in
the retrieval of dust properties. It should always be investigated whether obtained relationships are caused by natural phenomena
730 or artificially induced by model-inherent dependencies and a priori assumptions. In Sect. 6.3.4, similar as in Veselovskii et al.
(2020), dependencies of the S - δ relationship on the complex refractive index have been investigated under the assumption of
a fixed particle size and shape distribution. In addition, it was shown that changes in particle size and shape distribution have a
strong influence on the observed values and typically mask the effects of mineral composition (see Fig. 5).

The importance of a realistic representation of particle shape for the modeling of lidar-derived dust optical properties has
735 already been emphasized by Gasteiger et al. (2011). Since then, several model studies underlined the sensitivity of S and δ on
particle size and shape parameters, including surface roughness (e.g., Kemppinen et al., 2015; Bi et al., 2018; Saito and Yang,
2021; Kong et al., 2022). However, a comprehensive picture under consideration of various natural conditions is missing. In the
end, improvements of HETEAC for a better representation of dust particles will require further research based on a strong effort
of combining field and laboratory studies to evaluate potential scattering and shape models against real-world observations.
740 Size-, shape-, and composition-dependent spectral backscattering measurements at exactly 180° in the laboratory, such as
introduced by Miffre et al. (2022), are a prerequisite for the success of this work.

9 Conclusion and outlook

We have developed an aerosol classification model for the EarthCARE mission, which serves as the common baseline for
development, evaluation, and implementation of algorithms and can be used for the exploitation of measurement data later
745 on. The major feature of the model is the consistent end-to-end description of particle microphysical, optical, and radiative
properties. The model supports aerosol typing with ATLID and MSI and can be applied for radiation closure assessments
by using BBR measurements but also other spaceborne or surface data. Based on the heritage of previous typing approaches
and an advanced experimental data base from ground-based lidar measurements at multiple wavelengths, four basic aerosol
components containing weakly and strongly absorbing fine-mode as well as spherical and non-spherical coarse-mode particles
750 were selected to describe the aerosol microphysical properties. These components can be used to compose the major aerosol
types of anthropogenic pollution, smoke, marine aerosol, and dust as well as their mixtures. Size, shape, and refractive-index
parameters of the components were thoroughly adjusted to assure that the modeled optical properties cover the expected
observational phase space, in particular in terms of the EarthCARE observables lidar ratio, particle linear depolarization ratio,
and Ångström exponent. Mixing of the components allows the simulation of a wide range of natural conditions. In this way, it
755 is possible to link the optical fingerprints delivered by the spaceborne instruments to major pure and mixed aerosol types and
to assign respective radiative properties to the observed scenes.

The EarthCARE algorithms and products that are based on HETEAC will be carefully evaluated in the framework of the calibration and validation program of the mission. These activities shall help us identify and implement necessary improvements in both the HETEAC model itself and the algorithms that make use of it. A major focus of future development works will be on the harmonization of the EarthCARE aerosol data set with the long-term CALIPSO observations. HETEAC was designed such that a consistent aerosol typing for both missions will be possible. The aerosol types used in the EarthCARE target classification can be related to the respective CALIPSO types. However, simple projections are certainly not sufficient to investigate, e.g., long-term trends of anthropogenic and natural atmospheric aerosol load and associated radiative effects. Therefore, we propose a dedicated community effort for developing a sustainable conversion strategy applicable to global aerosol data sets. Wavelength conversions, thresholds in defining pure and mixed aerosol types, as well as the consequences of typing from either Level 1 (CALIOP) or Level 2 data (ATLID) must be considered. While EarthCARE aerosol typing builds on intensive, i.e., concentration-independent, particle properties, the selection criteria in the CALIPSO typing scheme make use of the strength of the aerosol signal, the surface type, and the layer elevation (Omar et al., 2009; Kim et al., 2018). Hence, refinements of the typing by using CALIPSO Level 2 data as well as the development of combined type- and location-dependent conversion schemes should be envisaged. All efforts must include also stratospheric aerosols (Tackett et al., 2023), which requires further HETEAC developments as well.

So far, HETEAC focuses only on the troposphere. Nevertheless, the ATLID L2a processors are able to deal with stratospheric aerosol, and preliminary typing categories are considered in the A-TC product (see Fig. 10). As for the troposphere, the categorization is based on two-dimensional Gaussian distributions of typical S and δ values known from the literature. Mean values of 55 sr and 45 % for volcanic ash, 40 sr and 3 % for sulfate aerosol, and 70 sr and 3 % for stratospheric smoke are considered in this typing scheme. As shown, e.g., by Ansmann et al. (2021) and Floutsi et al. (2022), the identification of stratospheric smoke, which has considerably different properties than tropospheric smoke, is challenging. Therefore, the stratospheric aerosol classification for EarthCARE needs further investigations and a full end-to-end implementation in HETEAC. For this purpose, it is planned to develop a HETEAC 2.0 version before the launch of EarthCARE. In general, HETEAC and the associated algorithms will be updated regularly based on EarthCARE validation studies, which will be performed during the entire lifetime of the mission.

Data availability. The HETEAC model input parameters and the look-up table for aerosol mixtures are available from <https://doi.org/10.5281/zenodo.7732338> (Wandinger et al., 2023a).

Author contributions. UW has developed the HETEAC model and drafted the manuscript. AAF, HB, MH, and AA worked on the experimental lidar data base and contributed to the definition of the model aerosol components. AAF created the look-up table for aerosol mixtures. DD and GvZ constructed the HETEAC-based scattering libraries for ECSIM and implemented the aerosol typing scheme in the A-PRO processor. ND, AH, and UW worked on the MSI-related aerosol typing issues. MH implemented aerosol typing parameters in the A-LAY

and AM-COL processors. SM and JC contributed with the parts related to the ACM-CAP and ACM-RT processors, respectively. All authors were involved in the discussions during the HETEAC development and contributed material and/or text to the manuscript.

790 *Competing interests.* UW is member of the editorial board of Atmospheric Measurement Techniques and co-editor of the Special Issue to which this paper contributes. The peer-review process was guided by an independent editor. The authors have no other competing interests to declare.

Acknowledgements. This work has been funded by ESA grants 4000112018/14/NL/CT (APRIL) and 4000134661/21/NL/AD (CARDINAL). Oleg Dubovik kindly provided the spheroid scattering model used in the developments and Stefan Horn helped in setting up the
795 calculations. We thank Tobias Wehr and Michael Eisinger for their continuous support over many years and the EarthCARE developer team for valuable discussions in various meetings.

The work on the revision of this manuscript was overshadowed by the sudden and unexpected passing of ESA's EarthCARE Mission Scientist Tobias Wehr. His tireless commitment to the mission and the science community around EarthCARE will not be forgotten.

References

- 800 Ansmann, A., Ohneiser, K., Chudnovsky, A., Baars, H., and Engelmann, R.: CALIPSO aerosol-typing scheme misclassified stratospheric fire smoke: Case study from the 2019 Siberian wildfire season, *Frontiers in Environmental Science*, 9, <https://doi.org/10.3389/fenvs.2021.769852>, 2021.
- Baars, H., Ansmann, A., Althausen, D., Engelmann, R., Heese, B., Muller, D., Artaxo, P., Paixao, M., Pauliquevis, T., and Souza, R.: Aerosol profiling with lidar in the Amazon Basin during the wet and dry season, *Journal of Geophysical Research: Atmospheres*, 117, 16, <https://doi.org/10.1029/2012jd018338>, 2012.
- 805 Baars, H., Kanitz, T., Engelmann, R., Althausen, D., Heese, B., Komppula, M., Preissler, J., Tesche, M., Ansmann, A., Wandinger, U., Lim, J. H., Ahn, J. Y., Stachlewska, I. S., Amiridis, V., Marinou, E., Seifert, P., Hofer, J., Skupin, A., Schneider, F., Bohlmann, S., Foth, A., Bley, S., Pfuller, A., Giannakaki, E., Lihavainen, H., Viisanen, Y., Hooda, R. K., Pereira, S. N., Bortoli, D., Wagner, F., Mattis, I., Janicka, L., Markowicz, K. M., Achtert, P., Artaxo, P., Pauliquevis, T., Souza, R. A. F., Sharma, V. P., van Zyl, P. G., Beukes, J. P., Sun, J. Y., Rohwer, E. G., Deng, R. R., Mamouri, R. E., and Zamorano, F.: An overview of the first decade of Polly(NET): an emerging network of automated Raman-polarization lidars for continuous aerosol profiling, *Atmospheric Chemistry and Physics*, 16, 5111–5137, <https://doi.org/10.5194/acp-16-5111-2016>, 2016.
- 810 Barker, H. W., Cole, J. N. S., Qu, Z., Villefranque, N., and Shephard, M.: Radiative closure assessment of retrieved cloud and aerosol properties for the EarthCARE mission: the ACMB-DF product, *Atmospheric Measurement Techniques*, this special issue, 2023.
- 815 Bi, L., Lin, W., Liu, D., and Zhang, K.: Assessing the depolarization capabilities of nonspherical particles in a super-ellipsoidal shape space, *Optics Express*, 26, 1726–1742, <https://doi.org/10.1364/OE.26.001726>, 2018.
- Bohlmann, S., Baars, H., Radenz, M., Engelmann, R., and Macke, A.: Ship-borne aerosol profiling with lidar over the Atlantic Ocean: from pure marine conditions to complex dust-smoke mixtures, *Atmospheric Chemistry and Physics*, 18, 9661–9679, <https://doi.org/10.5194/acp-18-9661-2018>, 2018.
- 820 Burton, S. P., Ferrare, R. A., Hostetler, C. A., Hair, J. W., Rogers, R. R., Obland, M. D., Butler, C. F., Cook, A. L., Harper, D. B., and Froyd, K. D.: Aerosol classification using airborne High Spectral Resolution Lidar measurements - methodology and examples, *Atmospheric Measurement Techniques*, 5, 73–98, <https://doi.org/10.5194/amt-5-73-2012>, 2012.
- Cappa, C. D., Onasch, T. B., Massoli, P., Worsnop, D. R., Bates, T. S., Cross, E. S., Davidovits, P., Hakala, J., Hayden, K. L., Jobson, B. T., Kolesar, K. R., Lack, D. A., Lerner, B. M., Li, S.-M., Mellon, D., Nuaaman, I., Olfert, J. S., Petäjä, T., Quinn, P. K., Song, C., Subramanian, R., Williams, E. J., and Zaveri, R. A.: Radiative absorption enhancements due to the mixing state of atmospheric black carbon, *Science*, 337, 1078–1081, <https://doi.org/10.1126/science.1223447>, 2012.
- 825 Cole, J. N. S., Barker, H. W., Qu, Z., Villefranque, N., and Shephard, M. W.: Broadband Radiative Quantities for the EarthCARE Mission: The ACM-COM and ACM-RT Products, *Atmospheric Measurement Techniques Discussions*, 2022, 1–37, <https://doi.org/10.5194/amt-2022-304>, 2022.
- 830 D’Almeida, G., Koepke, P., and Shettle, E.: *Atmospheric Aerosols: Global Climatology and Radiative Characteristics*, Studies in geophysical optics and remote sensing, A. Deepak Pub., <https://books.google.de/books?id=C1wRAQAIAAJ>, 1991.
- de Leeuw, G., Holzer-Popp, T., Bevan, S., Davies, W. H., Descloitres, J., Grainger, R. G., Griesfeller, J., Heckel, A., Kinne, S., Klüser, L., Kolmonen, P., Litvinov, P., Martynenko, D., North, P., Ovigneur, B., Pascal, N., Poulsen, C., Ramon, D., Schulz, M., Siddans, R., Sogacheva, L., Tanré, D., Thomas, G. E., Virtanen, T. H., von Hoyningen Huene, W., Vountas, M., and Pinnock, S.: Evaluation

- 835 of seven European aerosol optical depth retrieval algorithms for climate analysis, *Remote Sensing of Environment*, 162, 295–315, <https://doi.org/10.1016/j.rse.2013.04.023>, 2015.
- Deepak, A. and Gerber, H. E.: Report of the experts meeting on aerosols and their climatic effects, Report WCP-55, World Meteorological Organization, Geneva, 1983.
- Denjean, C., Caquineau, S., Desboeufs, K., Laurent, B., Maille, M., Quiñones Rosado, M., Vallejo, P., Mayol-Bracero, O. L., and Formenti, P.: Long-range transport across the Atlantic in summertime does not enhance the hygroscopicity of African mineral dust, *Geophysical Research Letters*, 42, 7835–7843, <https://doi.org/10.1002/2015GL065693>, 2015.
- 840 Di Biagio, C., Formenti, P., Balkanski, Y., Caponi, L., Cazaunau, M., Pangui, E., Journet, E., Nowak, S., Caquineau, S., Andreae, M. O., Kandler, K., Saeed, T., Piketh, S., Seibert, D., Williams, E., and Doussin, J.-F.: Global scale variability of the mineral dust long-wave refractive index: a new dataset of in situ measurements for climate modeling and remote sensing, *Atmospheric Chemistry and Physics*, 17, 1901–1929, <https://doi.org/10.5194/acp-17-1901-2017>, 2017.
- 845 Di Biagio, C., Formenti, P., Balkanski, Y., Caponi, L., Cazaunau, M., Pangui, E., Journet, E., Nowak, S., Andreae, M. O., Kandler, K., Saeed, T., Piketh, S., Seibert, D., Williams, E., and Doussin, J.-F.: Complex refractive indices and single-scattering albedo of global dust aerosols in the shortwave spectrum and relationship to size and iron content, *Atmospheric Chemistry and Physics*, 19, 15 503–15 531, <https://doi.org/10.5194/acp-19-15503-2019>, 2019.
- 850 Docter, N., Preusker, R., Filipitsch, F., Kritten, L., Schmidt, F., and Fischer, J.: Aerosol optical depth retrieval from the EarthCARE multi-spectral imager: the M-AOT product, *EGUsphere*, 2023, 1–31, <https://doi.org/10.5194/egusphere-2023-150>, 2023.
- Donovan, D., van Zadelhoff, G.-J., and Wang, P.: The ATLID L2a profile processor (A-AER, A-EBD, A-TC and A-ICE products), *Atmospheric Measurement Techniques*, this special issue, 2023a.
- Donovan, D. P., Kollias, P., Velázquez Blázquez, A., and van Zadelhoff, G.-J.: The Generation of EarthCARE L1 Test Data sets Using Atmospheric Model Data Sets, *EGUsphere*, 2023, 1–54, <https://doi.org/10.5194/egusphere-2023-384>, 2023b.
- 855 Dubovik, O., Sinyuk, A., Lapyonok, T., Holben, B. N., Mishchenko, M., Yang, P., Eck, T. F., Volten, H., Muñoz, O., Veihelmann, B., van der Zande, W. J., Leon, J.-F., Sorokin, M., and Slutsker, I.: Application of spheroid models to account for aerosol particle nonsphericity in remote sensing of desert dust, *Journal of Geophysical Research: Atmospheres*, 111, <https://doi.org/10.1029/2005JD006619>, 2006.
- Düsing, S., Ansmann, A., Baars, H., Corbin, J. C., Denjean, C., Gysel-Beer, M., Müller, T., Poulain, L., Siebert, H., Spindler, G., Tuch, T., Wehner, B., and Wiedensohler, A.: Measurement report: Comparison of airborne, in situ measured, lidar-based, and modeled aerosol optical properties in the central European background – identifying sources of deviations, *Atmospheric Chemistry and Physics*, 21, 16 745–16 773, <https://doi.org/10.5194/acp-21-16745-2021>, 2021.
- 860 Eisinger, M., Wehr, T., Kubota, T., Bernaerts, D., and Wallace, K.: The EarthCARE Mission - Science Data Processing Chain Overview, *Atmospheric Measurement Techniques*, this special issue, 2023.
- 865 Engelmann, R., Kanitz, T., Baars, H., Heese, B., Althausen, D., Skupin, A., Wandinger, U., Komppula, M., Stachlewska, I. S., Amiridis, V., Marinou, E., Mattis, I., Linne, H., and Ansmann, A.: The automated multiwavelength Raman polarization and water-vapor lidar Polly(XT): the neXT generation, *Atmospheric Measurement Techniques*, 9, 1767–1784, <https://doi.org/10.5194/amt-9-1767-2016>, 2016.
- Fell, F. and Fischer, J.: Numerical simulation of the light field in the atmosphere–ocean system using the matrix-operator method, *Journal of Quantitative Spectroscopy and Radiative Transfer*, 69, 351–388, [https://doi.org/10.1016/S0022-4073\(00\)00089-3](https://doi.org/10.1016/S0022-4073(00)00089-3), 2001.
- 870 Floutsis, A. A., Baars, H., Engelmann, R., Althausen, D., Ansmann, A., Bohlmann, S., Heese, B., Hofer, J., Kanitz, T., Haarig, M., Ohneiser, K., Radenz, M., Seifert, P., Skupin, A., Yin, Z., Abdullaev, S. F., Komppula, M., Filioglou, M., Giannakaki, E., Stachlewska, I. S., Janicka, L., Bortoli, D., Marinou, E., Amiridis, V., Gialitaki, A., Mamouri, R.-E., Barja, B., and Wandinger, U.: DeLiAn – a growing collection

- of depolarization ratio, lidar ratio and Ångström exponent for different aerosol types and mixtures from ground-based lidar observations, *Atmospheric Measurement Techniques Discussions*, 2022, 1–39, <https://doi.org/10.5194/amt-2022-306>, 2022.
- 875 Floutsi, A. A., Baars, H., Engelmann, R., Althausen, D., Ansmann, A., Bohlmann, S., Heese, B., Hofer, J., Kanitz, T., Haarig, M., Ohneiser, K., Radenz, M., Seifert, P., Skupin, A., Yin, Z., Abdullaev, S. F., Komppula, M., Filioglou, M., Giannakaki, E., Stachlewska, I. S., Janicka, L., Bortoli, D., Marinou, E., Amiridis, V., Gialitaki, A., Mamouri, R.-E., Barja, B., and Wandinger, U.: DeLiAn – a growing collection of depolarization ratio, lidar ratio and Ångström exponent for different aerosol types and mixtures from ground-based lidar observations, <https://doi.org/10.5281/zenodo.7751752>, 2023.
- 880 Gasteiger, J., Wiegner, M., Groß, S., Freudenthaler, V., Toledano, C., Tesche, M., and Kandler, K.: Modelling lidar-relevant optical properties of complex mineral dust aerosols, *Tellus B*, 63, 725–741, <https://doi.org/10.1111/j.1600-0889.2011.00559.x>, 2011.
- Giannakaki, E., Pfüller, A., Korhonen, K., Mielonen, T., Laakso, L., Vakkari, V., Baars, H., Engelmann, R., Beukes, J. P., Van Zyl, P. G., Josipovic, M., Tiitta, P., Chiloane, K., Piketh, S., Lihavainen, H., Lehtinen, K. E. J., and Komppula, M.: One year of Raman lidar observations of free-tropospheric aerosol layers over South Africa, *Atmospheric Chemistry and Physics*, 15, 5429–5442, <https://doi.org/10.5194/acp-15-5429-2015>, 2015.
- 885 Groß, S., Freudenthaler, V., Wirth, M., and Weinzierl, B.: Towards an aerosol classification scheme for future EarthCARE lidar observations and implications for research needs, *Atmospheric Science Letters*, 16, 77–82, <https://doi.org/10.1002/asl2.524>, 2015.
- Groß, S., Tesche, M., Freudenthaler, V., Toledano, C., Wiegner, M., Ansmann, A., Althausen, D., and Seefeldner, M.: Characterization of Saharan dust, marine aerosols and mixtures of biomass-burning aerosols and dust by means of multi-wavelength depolarization and Raman lidar measurements during SAMUM-2, *Tellus B*, 63, 706–724, <https://doi.org/10.1111/j.1600-0889.2011.00556.x>, 2011.
- 890 Haarig, M., Ansmann, A., Althausen, D., Klepel, A., Groß, S., Freudenthaler, V., Toledano, C., Mamouri, R.-E., Farrell, D. A., Prescod, D. A., Marinou, E., Burton, S. P., Gasteiger, J., Engelmann, R., and Baars, H.: Triple-wavelength depolarization-ratio profiling of Saharan dust over Barbados during SALTRACE in 2013 and 2014, *Atmospheric Chemistry and Physics*, 17, 10767–10794, <https://doi.org/10.5194/acp-17-10767-2017>, 2017a.
- 895 Haarig, M., Ansmann, A., Gasteiger, J., Kandler, K., Althausen, D., Baars, H., Radenz, M., and Farrell, D. A.: Dry versus wet marine particle optical properties: RH dependence of depolarization ratio, backscatter, and extinction from multiwavelength lidar measurements during SALTRACE, *Atmospheric Chemistry and Physics*, 17, 14199–14217, <https://doi.org/10.5194/acp-17-14199-2017>, 2017b.
- Haarig, M., Ansmann, A., Baars, H., Jimenez, C., Veselovskii, I., Engelmann, R., and Althausen, D.: Depolarization and lidar ratios at 355, 532, and 1064 nm and microphysical properties of aged tropospheric and stratospheric Canadian wildfire smoke, *Atmospheric Chemistry and Physics*, 18, 11847–11861, <https://doi.org/10.5194/acp-18-11847-2018>, 2018.
- 900 Haarig, M., Ansmann, A., Engelmann, R., Baars, H., Toledano, C., Torres, B., Althausen, D., Radenz, M., and Wandinger, U.: First triple-wavelength lidar observations of depolarization and extinction-to-backscatter ratios of Saharan dust, *Atmospheric Chemistry and Physics*, 22, 355–369, <https://doi.org/10.5194/acp-22-355-2022>, 2022.
- Haarig, M., Hünnerbein, A., Wandinger, U., Docter, N., Preusker, R., Horn, S., Schneider, F., Donovan, D., and van Zadelhoff, G.-J.: Cloud top heights and aerosol columnar properties from combined EarthCARE lidar and imager observations: the AM-CTH and AM-ACD products, *Atmospheric Measurement Techniques*, this special issue, 2023.
- 905 Hamill, P., Giordano, M., Ward, C., Giles, D., and Holben, B.: An AERONET-based aerosol classification using the Mahalanobis distance, *Atmospheric Environment*, 140, 213–233, <https://doi.org/10.1016/j.atmosenv.2016.06.002>, 2016.
- Hess, M., Koepke, P., and Schult, I.: Optical properties of aerosols and clouds: The software package OPAC, *Bulletin of the American Meteorological Society*, 79, 831–844, [https://doi.org/10.1175/1520-0477\(1998\)079<0831:OPOAAC>2.0.CO;2](https://doi.org/10.1175/1520-0477(1998)079<0831:OPOAAC>2.0.CO;2), 1998.
- 910

- Hofer, J., Ansmann, A., Althausen, D., Engelmann, R., Baars, H., Fomba, K. W., Wandinger, U., Abdullaev, S. F., and Makhmudov, A. N.: Optical properties of Central Asian aerosol relevant for spaceborne lidar applications and aerosol typing at 355 and 532 nm, *Atmospheric Chemistry and Physics*, 20, 9265–9280, <https://doi.org/10.5194/acp-20-9265-2020>, 2020.
- 915 Holben, B., Eck, T., Slutsker, I., Tanré, D., Buis, J., Setzer, A., Vermote, E., Reagan, J., Kaufman, Y., Nakajima, T., Lavenu, F., Jankowiak, I., and Smirnov, A.: AERONET – A federated instrument network and data archive for aerosol characterization, *Remote Sensing of Environment*, 66, 1–16, [https://doi.org/10.1016/S0034-4257\(98\)00031-5](https://doi.org/10.1016/S0034-4257(98)00031-5), 1998.
- Hollstein, A. and Fischer, J.: Radiative transfer solutions for coupled atmosphere ocean systems using the matrix operator technique, *Journal of Quantitative Spectroscopy and Radiative Transfer*, 113, 536–548, <https://doi.org/10.1016/j.jqsrt.2012.01.010>, 2012.
- 920 Holzer-Popp, T., de Leeuw, G., Griesfeller, J., Martynenko, D., Klüser, L., Bevan, S., Davies, W., Ducos, F., Deuzé, J. L., Grainger, R. G., Heckel, A., von Hoyningen-Hüne, W., Kolmonen, P., Litvinov, P., North, P., Poulsen, C. A., Ramon, D., Siddans, R., Sogacheva, L., Tanre, D., Thomas, G. E., Vountas, M., Descloitres, J., Griesfeller, J., Kinne, S., Schulz, M., and Pinnock, S.: Aerosol retrieval experiments in the ESA Aerosol_cci project, *Atmospheric Measurement Techniques*, 6, 1919–1957, <https://doi.org/10.5194/amt-6-1919-2013>, 2013.
- Hänel, G. and Zankl, B.: Aerosol size and relative humidity: Water uptake by mixtures of salts, *Tellus*, 31, 478–486, <https://doi.org/10.1111/j.2153-3490.1979.tb00929.x>, 1979.
- 925 Iacono, M. J., Delamere, J. S., Mlawer, E. J., Shephard, M. W., Clough, S. A., and Collins, W. D.: Radiative forcing by long-lived greenhouse gases: Calculations with the AER radiative transfer models, *Journal of Geophysical Research: Atmospheres*, 113, <https://doi.org/10.1029/2008JD009944>, 2008.
- Illingworth, A. J., Barker, H. W., Beljaars, A., Ceccaldi, M., Chepfer, H., Clerbaux, N., Cole, J., Delanoë, J., Domenech, C., Donovan, D. P., Fukuda, S., Hiraoka, M., Hogan, R. J., Huenerbein, A., Kollias, P., Kubota, T., Nakajima, T., Nakajima, T. Y., Nishizawa, T., Ohno, Y., 930 Okamoto, H., Oki, R., Sato, K., Satoh, M., Shephard, M. W., Velazquez-Blazquez, A., Wandinger, U., Wehr, T., and van Zadelhoff, G. J.: The EarthCARE satellite – The next step forward in global measurements of clouds, aerosols, precipitation, and radiation, *Bulletin of the American Meteorological Society*, 96, 1311–1332, <https://doi.org/10.1175/bams-d-12-00227.1>, 2015.
- Irbah, A., Delanoë, J., van Zadelhoff, G.-J., Donovan, D. P., Kollias, P., Puigdomènech Treserras, B., Mason, S., Hogan, R. J., and Tatarevic, A.: The classification of atmospheric hydrometeors and aerosols from the EarthCARE radar and lidar: the A-TC, C-TC and AC-TC 935 products, *EGUsphere*, 2022, 1–31, <https://doi.org/10.5194/egusphere-2022-1217>, 2022.
- Jacobson, M. Z.: A physically-based treatment of elemental carbon optics: Implications for global direct forcing of aerosols, *Geophysical Research Letters*, 27, 217–220, <https://doi.org/10.1029/1999GL010968>, 2000.
- Jacobson, M. Z.: Strong radiative heating due to the mixing state of black carbon in atmospheric aerosols, *Nature*, 409, 695–697, <https://doi.org/10.1038/35055518>, 2001.
- 940 Kandler, K., Schütz, L., Deutscher, C., Ebert, M., Hofmann, H., Jäckel, S., Jaenicke, R., Knippertz, P., Lieke, K., Massling, A., Petzold, A., Schladitz, A., Weinzierl, B., Wiedensohler, A., Zorn, S., and Weinbruch, S.: Size distribution, mass concentration, chemical and mineralogical composition and derived optical parameters of the boundary layer aerosol at Tinfou, Morocco, during SAMUM 2006, *Tellus B*, 61, 32–50, <https://doi.org/10.1111/j.1600-0889.2008.00385.x>, 2009.
- Kanitz, T., Ansmann, A., Seifert, P., Engelmann, R., Kalisch, J., and Althausen, D.: Radiative effect of aerosols above the northern and 945 southern Atlantic Ocean as determined from shipborne lidar observations, *Journal of Geophysical Research: Atmospheres*, 118, 12,556–12,565, <https://doi.org/10.1002/2013JD019750>, 2013.
- Kanitz, T., Engelmann, R., Heinold, B., Baars, H., Skupin, A., and Ansmann, A.: Tracking the Saharan Air Layer with shipborne lidar across the tropical Atlantic, *Geophysical Research Letters*, 41, 1044–1050, <https://doi.org/10.1002/2013GL058780>, 2014.

- Kemppinen, O., Nousiainen, T., and Lindqvist, H.: The impact of surface roughness on scattering by realistically shaped wavelength-scale dust particles, *Journal of Quantitative Spectroscopy and Radiative Transfer*, 150, 55–67, <https://doi.org/10.1016/j.jqsrt.2014.05.024>, 2015.
- 950 Kim, M.-H., Omar, A. H., Tackett, J. L., Vaughan, M. A., Winker, D. M., Trepte, C. R., Hu, Y., Liu, Z., Poole, L. R., Pitts, M. C., Kar, J., and Magill, B. E.: The CALIPSO version 4 automated aerosol classification and lidar ratio selection algorithm, *Atmospheric Measurement Techniques*, 11, 6107–6135, <https://doi.org/10.5194/amt-11-6107-2018>, 2018.
- Koepke, P., Gasteiger, J., and Hess, M.: Technical Note: Optical properties of desert aerosol with non-spherical mineral particles: data incorporated to OPAC, *Atmospheric Chemistry and Physics*, 15, 5947–5956, <https://doi.org/10.5194/acp-15-5947-2015>, 2015.
- 955 Kong, S., Sato, K., and Bi, L.: Lidar ratio–depolarization ratio relations of atmospheric dust aerosols: The super-spheroid model and High Spectral Resolution Lidar observations, *Journal of Geophysical Research: Atmospheres*, 127, e2021JD035629, <https://doi.org/10.1029/2021JD035629>, 2022.
- Köpke, P., Hess, M., Schult, I., and Shettle, E. P.: Global aerosol data set, Report 243, Max-Planck-Institut für Meteorologie, <http://hdl.handle.net/21.11116/0000-0009-EB9B-0>, 1997.
- 960 Lesins, G., Chylek, P., and Lohmann, U.: A study of internal and external mixing scenarios and its effect on aerosol optical properties and direct radiative forcing, *Journal of Geophysical Research: Atmospheres*, 107, AAC 5–1–AAC 5–12, <https://doi.org/10.1029/2001JD000973>, 2002.
- Li, J., Carlson, B. E., Yung, Y. L., Lv, D., Hansen, J., Penner, J. E., Liao, H., Ramaswamy, V., Kahn, R. A., Zhang, P., Dubovik, O., Ding, A., 965 Lacis, A. A., Zhang, L., and Dong, Y.: Scattering and absorbing aerosols in the climate system, *Nature Reviews Earth & Environment*, 3, 363–379, <https://doi.org/10.1038/s43017-022-00296-7>, 2022.
- Mason, S. L., Hogan, R. J., Bozzo, A., and Pounder, N. L.: A unified synergistic retrieval of clouds, aerosols and precipitation from Earth-CARE: the ACM-CAP product, *EGU_{sphere}*, 2022, 1–41, <https://doi.org/10.5194/egusphere-2022-1195>, 2022.
- Miffre, A., Cholleton, D., Noël, C., and Rairoux, P.: Investigating the dependence of mineral dust depolarization on complex refractive index and size with a laboratory polarimeter at 180.0° lidar backscattering angle, *Atmospheric Measurement Techniques Discussions*, 2022, 970 1–24, <https://doi.org/10.5194/amt-2022-192>, 2022.
- Mishchenko, M. I. and Travis, L. D.: Capabilities and limitations of a current FORTRAN implementation of the T-matrix method for randomly oriented, rotationally symmetric scatterers, *Journal of Quantitative Spectroscopy and Radiative Transfer*, 60, 309–324, [https://doi.org/10.1016/S0022-4073\(98\)00008-9](https://doi.org/10.1016/S0022-4073(98)00008-9), 1998.
- 975 Mishchenko, M. I., Travis, L. D., and Lacis, A. A.: *Scattering, Absorption, and Emission of Light by Small Particles*, Cambridge University Press, Cambridge, 2002.
- Müller, T., Schladitz, A., Massling, A., Kaaden, N., Kandler, K., and Wiedensohler, A.: Spectral absorption coefficients and imaginary parts of refractive indices of Saharan dust during SAMUM-1, *Tellus B*, 61, 79–95, <https://doi.org/10.1111/j.1600-0889.2008.00399.x>, 2009.
- Nicolae, D., Vasilescu, J., Talianu, C., Biniotoglou, I., Nicolae, V., Andrei, S., and Antonescu, B.: A neural network aerosol-typing algorithm based on lidar data, *Atmospheric Chemistry and Physics*, 18, 14511–14537, <https://doi.org/10.5194/acp-18-14511-2018>, 2018.
- 980 Nishizawa, T., Sugimoto, N., Matsui, I., Shimizu, A., Hara, Y., Itsushi, U., Yasunaga, K., Kudo, R., and Kim, S.-W.: Ground-based network observation using Mie–Raman lidars and multi-wavelength Raman lidars and algorithm to retrieve distributions of aerosol components, *Journal of Quantitative Spectroscopy and Radiative Transfer*, 188, 79–93, <https://doi.org/10.1016/j.jqsrt.2016.06.031>, 2017.
- Omar, A., Won, J., Winker, D., Yoon, S., Dubovik, O., and McCormick, M.: Development of global aerosol models using cluster analysis of Aerosol Robotic Network (AERONET) measurements, *Journal of Geophysical Research: Atmospheres*, 110, 985 <https://doi.org/10.1029/2004JD004874>, 2005.

- Omar, A. H., Winker, D. M., Vaughan, M. A., Hu, Y., Treppe, C. R., Ferrare, R. A., Lee, K.-P., Hostetler, C. A., Kittaka, C., Rogers, R. R., Kuehn, R. E., and Liu, Z.: The CALIPSO automated aerosol classification and lidar ratio selection algorithm, *Journal of Atmospheric and Oceanic Technology*, 26, 1994–2014, <https://doi.org/10.1175/2009JTECHA1231.1>, 2009.
- 990 Papagiannopoulos, N., Mona, L., Amodeo, A., D’Amico, G., Gumà Claramunt, P., Pappalardo, G., Alados-Arboledas, L., Guerrero-Rascado, J. L., Amiridis, V., Kokkalis, P., Apituley, A., Baars, H., Schwarz, A., Wandinger, U., Biniotoglou, I., Nicolae, D., Bortoli, D., Comerón, A., Rodríguez-Gómez, A., Sicard, M., Papayannis, A., and Wiegner, M.: An automatic observation-based aerosol typing method for EARLINET, *Atmospheric Chemistry and Physics*, 18, 15 879–15 901, <https://doi.org/10.5194/acp-18-15879-2018>, 2018.
- Pappalardo, G., Amodeo, A., Apituley, A., Comeron, A., Freudenthaler, V., Linné, H., Ansmann, A., Bösenberg, J., D’Amico, G., Mattis, I., 995 Mona, L., Wandinger, U., Amiridis, V., Alados-Arboledas, L., Nicolae, D., and Wiegner, M.: EARLINET: towards an advanced sustainable European aerosol lidar network, *Atmospheric Measurement Techniques*, 7, 2389–2409, <https://doi.org/10.5194/amt-7-2389-2014>, 2014.
- Petzold, A., Rasp, K., Weinzierl, B., Esselborn, M., Hamburger, T., Dörnbrack, A., Kandler, K., Schütz, L., Knippertz, P., Fiebig, M., and Virkkula, A.: Saharan dust absorption and refractive index from aircraft-based observations during SAMUM 2006, *Tellus B*, 61, 118–130, <https://doi.org/10.1111/j.1600-0889.2008.00383.x>, 2009.
- 1000 Qu, Z., Barker, H. W., Cole, J. N. S., and Shephard, M. W.: Across-track Extension of Retrieved Cloud and Aerosol Properties for the Earth-CARE Mission: The ACM-3D Product, *Atmospheric Measurement Techniques Discussions*, 2022, 1–28, <https://doi.org/10.5194/amt-2022-301>, 2022a.
- Qu, Z., Donovan, D. P., Barker, H. W., Cole, J. N. S., Shephard, M. W., and Huijnen, V.: Numerical Model Generation of Test Frames for Pre-launch Studies of EarthCARE’s Retrieval Algorithms and Data Management System, *Atmospheric Measurement Techniques Discussions*, 1005 2022, 1–31, <https://doi.org/10.5194/amt-2022-300>, 2022b.
- Rittmeister, F., Ansmann, A., Engelmann, R., Skupin, A., Baars, H., Kanitz, T., and Kinne, S.: Profiling of Saharan dust from the Caribbean to western Africa – Part I: Layering structures and optical properties from shipborne polarization/Raman lidar observations, *Atmospheric Chemistry and Physics*, 17, 12 963–12 983, <https://doi.org/10.5194/acp-17-12963-2017>, 2017.
- Russell, P. B., Kacenelenbogen, M., Livingston, J. M., Hasekamp, O. P., Burton, S. P., Schuster, G. L., Johnson, M. S., Knobelspiesse, K. D., 1010 Redemann, J., Ramachandran, S., and Holben, B.: A multiparameter aerosol classification method and its application to retrievals from spaceborne polarimetry, *Journal of Geophysical Research: Atmospheres*, 119, 9838–9863, <https://doi.org/10.1002/2013JD021411>, 2014.
- Saito, M. and Yang, P.: Advanced Bulk Optical Models Linking the Backscattering and Microphysical Properties of Mineral Dust Aerosol, *Geophysical Research Letters*, 48, e2021GL095 121, <https://doi.org/10.1029/2021GL095121>, 2021.
- Schuster, G. L., Vaughan, M., MacDonnell, D., Su, W., Winker, D., Dubovik, O., Lapyonok, T., and Treppe, C.: Comparison of CALIPSO 1015 aerosol optical depth retrievals to AERONET measurements, and a climatology for the lidar ratio of dust, *Atmospheric Chemistry and Physics*, 12, 7431–7452, <https://doi.org/10.5194/acp-12-7431-2012>, 2012.
- Shettle, E. P. and Fenn, R. W.: Models for the aerosols of the lower atmosphere and the effects of humidity variations on their optical properties, Tech. rep., Air Force Geophysics Laboratory, 1979.
- Tackett, J. L., Kar, J., Vaughan, M. A., Getzewich, B. J., Kim, M.-H., Vernier, J.-P., Omar, A. H., Magill, B. E., Pitts, M. C., and Winker, 1020 D. M.: The CALIPSO version 4.5 stratospheric aerosol subtyping algorithm, *Atmospheric Measurement Techniques*, 16, 745–768, <https://doi.org/10.5194/amt-16-745-2023>, 2023.
- Tesche, M., Ansmann, A., Müller, D., Althausen, D., Mattis, I., Heese, B., Freudenthaler, V., Wiegner, M., Esselborn, M., Pisani, G., and Knippertz, P.: Vertical profiling of Saharan dust with Raman lidars and airborne HSRL in southern Morocco during SAMUM, *Tellus B*, 61, 144–164, <https://doi.org/10.1111/j.1600-0889.2008.00390.x>, 2009a.

- 1025 Tesche, M., Ansmann, A., Müller, D., Althausen, D., Engelmann, R., Freudenthaler, V., and Groß, S.: Vertically resolved separation of dust and smoke over Cape Verde using multiwavelength Raman and polarization lidars during Saharan Mineral Dust Experiment 2008, *Journal of Geophysical Research: Atmospheres*, 114, 14, <https://doi.org/10.1029/2009jd011862>, 2009b.
- Thomas, M. A., Devasthale, A., and Kahnert, M.: Marine aerosol properties over the Southern Ocean in relation to the wintertime meteorological conditions, *Atmospheric Chemistry and Physics*, 22, 119–137, <https://doi.org/10.5194/acp-22-119-2022>, 2022.
- 1030 Veselovskii, I., Hu, Q., Goloub, P., Podvin, T., Korenskiy, M., Derimian, Y., Legrand, M., and Castellanos, P.: Variability in lidar-derived particle properties over West Africa due to changes in absorption: towards an understanding, *Atmospheric Chemistry and Physics*, 20, 6563–6581, <https://doi.org/10.5194/acp-20-6563-2020>, 2020.
- Wandinger, U., Baars, H., Engelmann, R., Hünerbein, A., Horn, S., Kanitz, T., Donovan, D., van Zadelhoff, G.-J., Daou, D., Fischer, J., von Bismarck, J., Filipitsch, F., Docter, N., Eisinger, M., Lajas, D., and Wehr, T.: HETEAC: The aerosol classification model for EarthCARE, *EPJ Web of Conferences*, 119, 01 004, <https://doi.org/10.1051/epjconf/201611901004>, 2016.
- 1035 Wandinger, U., Floutsi, A. A., Baars, H., Haarig, M., Ansmann, A., Hünerbein, A., Docter, N., Donovan, D., van Zadelhoff, G.-J., Mason, S., and Cole, J.: HETEAC – The Hybrid End-To-End Aerosol Classification model for EarthCARE: Look-Up Table (LUT) for aerosol mixtures, <https://doi.org/10.5281/zenodo.7732338>, 2023a.
- Wandinger, U., Haarig, M., Baars, H., Donovan, D., and van Zadelhoff, G.-J.: Cloud top heights and aerosol layer properties from EarthCARE
1040 lidar observations: the A-CTH and A-ALD products, *Atmospheric Measurement Techniques*, this special issue, 2023b.
- Wehr, T., Kubota, T., Tzeremes, G., Wallace, K., Nakatsuka, H., Ohno, Y., Koopman, R., Rusli, S., Kikuchi, M., Eisinger, M., Tanaka, T., Taga, M., Deghaye, P., Tomita, E., and Bernaerts, D.: The EarthCARE Mission – Science and System Overview, *EGUsphere*, 2023, 1–47, <https://doi.org/10.5194/egusphere-2022-1476>, 2023.
- Yang, P. and Liou, K.: Geometric-optics-integral-equation method for light scattering by nonspherical ice crystals, *Applied Optics*, 35,
1045 6568–6584, <https://doi.org/10.1364/ao.35.006568>, 1996.
- Zieger, P., Fierz-Schmidhauser, R., Weingartner, E., and Baltensperger, U.: Effects of relative humidity on aerosol light scattering: results from different European sites, *Atmospheric Chemistry and Physics*, 13, 10 609–10 631, <https://doi.org/10.5194/acp-13-10609-2013>, 2013.